A detector to monitor the neutrino beam asymmetry at the T2K 280m hall

September 8, 2008

Abstract

We propose to build and operate a new detector for the T2K 280m hall with the purpose of measuring and monitoring the possible neutrino beam left-right asymmetry with respect to the beam axis. The measurement will be performed by means of two identical detectors (modules) made of a sandwich of iron plates and planes of scintillator bars read out by WLS fibers and multianode PMTs. The two modules could be swapped in their positions in order to minimize systematic errors. We show that an overall uncertainty of less than 5 % in the measurement of the beam asymmetry could be reached within one year of running.

2KM Left-Right monitor subgroup

LHEP, University of Bern, Switzerland:
A. Ariga, F. Bay, A. Ereditato, E. Frank, M. Hess, M. Messina, H.-U. Schütz

IN2P3, IPN Lyon, France:
D. Autiero, B. Carlus, A. Cazes, L. Chaussard, Y. Declais, S. Gardien, C. Girerd, C. Guerin, J. Marteau

ICRR, University of Tokyo, Kashiwa-shi, Chiba, 277-8582, Japan:
S. Hazama, C. Ishihara, H. Kaji, T. Kajita, K. Kaneyuki, K. Okumura, Y. Shimizu, N. Tanimoto

Contents

1 Introduction and physics motivation

There is now a strong consensus that neutrino flavor states mix with each other and undergo oscillations. The next generation of experiments must begin making precision measurements of the known neutrino oscillation parameters and attempt to measure the currently unknown parameters. The T2K (Tokai-to-Kamioka) neutrino oscillation experiment will start taking data in 2009 and its goals are:

- to observe ν_e appearance;
- to measure $\sin^2 2\theta_{23}$ to better than the few percent level;
- to measure $\sin^2 2\theta_{13}$ or improve the limit by a factor of 10 to 20.

The experiment includes, in addition to the far Super-K detector, a near detector in the 280 m hall and the possibility for a 2 km detector site. As we have already discussed in the 2KM letter of intent [1], the background estimation of the electron neutrino measurement at Super-K is crucial to observe ν_e appearance at Super-K.

All of the elements of the T2K experiment, either existing, under construction or proposed, are shown in figure 1. T2K will use an off-axis beam to produce a sharp peak in the energy spectrum of neutrinos

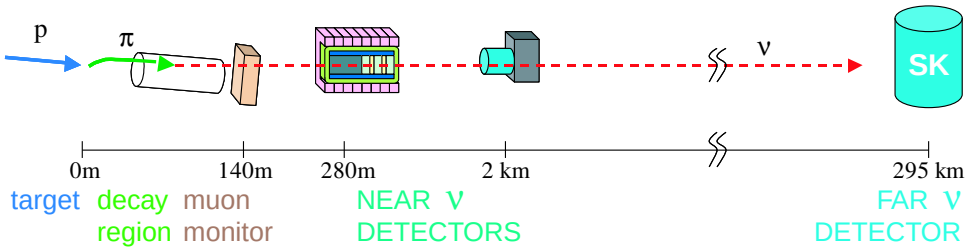

Figure 1: Sketch of the elements of the T2K experiment. The auxiliary CERN T2K/NA61 pion production experiment will be used to predict the pion momentum in the decay region.

at the ν oscillation maximum energy. This will maximize the signatures of ν_μ disappearance and the ν_e appearance. Since the part of the neutrino beam flux measured by Super-K is only a small portion of the entire beam, the neutrino energy spectrum seen at Super-K is quite different from the energy spectrum of the initial beam. Even along the off-axis angle, the finite size of any detector subtends a different fraction of the beam depending on the size of the detector and on the distance from the production point. This is shown in figure 2 where we compare the neutrino beam spectrum 2 degrees off-axis for the anticipated detectors at 280 m, at approximately 2 km and at 295 km.

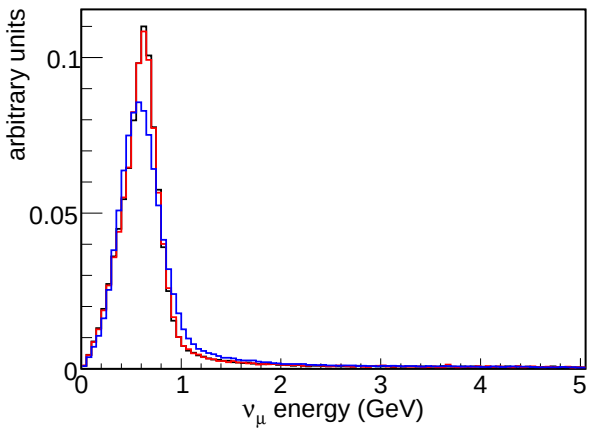

Figure 2: Expected T2K neutrino flux at 280 m (blue line), 2 km (red line), and Super-K (black) line.

Although the proposed detector at 2 km subtends a solid angle 30 times larger than Super-K at 295 km, it is distant enough that the neutrino energy spectrum at the 2KM and Super-K sites are similar in shape. The differences in flux as measured at 280 m and 295 km can be seen more clearly by looking at the ratio of "near" ν_μ flux to the "far" flux (N/F ratio) as a function of energy. The left and right panels of figure 3 show this ratio at 280 m and 2 km respectively. Since the energy of the peak positions is shifted at 280 m relative to that at Super-K, the N/F ratio drastically changes in the region of the oscillation maximum. On the other hand, we can see that by moving to about 2 km, the N/F ratio is flat at the 5 % level.

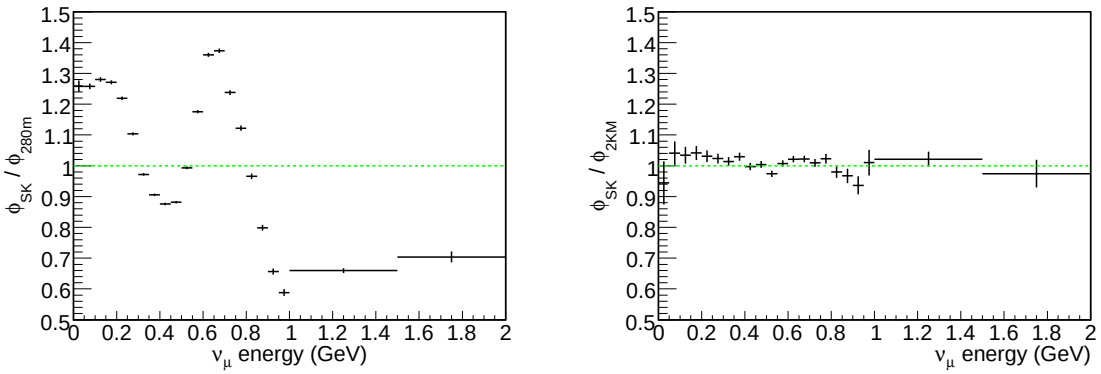

Figure 3: Near/Far neutrino flux ratio as a function of energy at 280 m (left) and 2 km (right) from the T2K target.

Using both the results from the T2K/NA61 experiment at CERN and the detector at 280 m will provide a prediction of the unoscillated flux at Super-K. This prediction can be directly checked by the 2KM detector since it has the same technology and target as Super-K and since the flux seen at the 2KM site is almost the same as the one seen at Super-K in the absence of oscillations.

The candidate site for the 2KM detector is at 2.5 degrees off-axis, which is not on the line from the target to Super-K, but on a symmetric line with respect to the beam direction. This is due to the cheaper excavation available at this location. Even if the beam center is well measured and tuned to the center of the on-axis detector it doesn't ensure the symmetry of flux at the left- and right positions. Therefore, one needs to monitor the symmetry of the neutrino beam profile before it reaches the 2KM site. Figure 4 shows the relative locations of the target. We propose to install two identical detectors, the Left-Right monitor, to measure the neutrino flux in two directions.

The Left-Right monitor will measure the left and right neutrino beam profile simultaneously with two identical modules in the T2K 280m hall. Figure 5 shows a 3D view of the 280m hall. The magnet of the ND280 detector is located at the center of the hall. The Left-Right monitors will be installed in symmetric places: one located downstream of the magnet (the Right monitor), the other on the side of the magnet (the Left monitor), as shown in the figure. Figure 6 shows the top view of the B1 floor where the ND280 detector and the Left-Right monitor will be installed. The side view of the hall is shown in figure 7, where the INGRID detector is at the beam center, while the ND280 and the Left-Right detectors are at off-axis position.

As anticipated, the goal of the Left-Right detector is to measure the off-axis, left-right asymmetry with an accuracy better than 5 % within one year. In order to achieve this goal:

- at least 10^5 fully contained events per year are required
- the detector must cover neutrinos in the signal region $0.2 < E_\nu < 1$ GeV (see figure 2 of the expected neutrino spectrum at 280m, 2KM and Super-K sites)
- the total systematic uncertainties should be 5 % or smaller.

In order to fulfill these requirements with a detector of limited space (2×2 m^2) and weight (< 5 t) (see figures 6 and 7), we propose a simple sandwich structure using scintillators and iron plates.

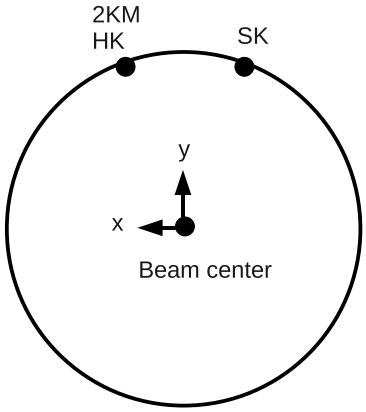

Figure 4: Transverse position of the T2K neutrino beam relative to 2KM, Super-K and the possible future Hyper-K detector with respect to the target. The circle represents the 2.5 degrees off-axis angle from the beam. In this configuration all detectors are off-axis. The proposed Left-Right monitors would be installed in the 280 m hall along the same directions as the 2KM and Super-K detectos.

The neutrino detection principle of the monitor is similar to that of INGRID, which is based on a ranged measurement of muons produced by charged current (CC) neutrino interactions. Since the energy of the off-axis neutrino flux is lower than the one on-axis, the Left-Right monitor needs higher sensitivity to lower energy neutrinos than INGRID. This goal can be achieved using thinner iron plates. The iron plates, in particular those of the Right monitor, do not affect the magnetic field of the ND280 magnet which has been checked in simulation.

The Left-Right monitor will be used not only to measure the cumulative difference between the left and right neutrino flux but also to monitor the long term stability of the beam symmetry. The detector basically measures fully contained muons in order to reconstruct the neutrino energy. Due to its finite size, muons with momentum higher than 1 GeV/c escape from the detection volume. Information on higher energy neutrinos will be inferred from the detection of partially contained muons.

The neutral current (NC) interaction of high energy neutrinos is expected to be a significant background for the Super-K and the 2KM detector. Therefore, it will be also important to perform the symmetry measurement at high energies.

The role of the Left-Right monitor is complementary to that of INGRID, which will monitor the direction of the on-axis neutrino beam with a precision better than 1 mrad. This information is needed by the Left-Right monitor to estimate the asymmetry caused by the beam direction. On the other hand, the Left-Right monitor will provide the neutrino flux at two points that are not covered by INGRID. It will help constrain the beam Monte-Carlo simulation and flux corrections independently of the 2KM detector. Although the Left-Right monitor can solely measure the beam asymmetry after confirmation of the beam position by INGRID, it requires a precise measurement of neutrino interactions at the ND280 detector to minimize systematic uncertainties. The ND280 detector will provide the cross-section and the energy distribution of the neutrino beam. The results of the ND280 detector let us know the fraction of CC and NC neutrino interactions at all energies. Then, we can reduce systematic uncertainties in the left-right flux measurement due to the contamination of NC and other CC events in the CC quasi-elastic (CCQE) interaction events.

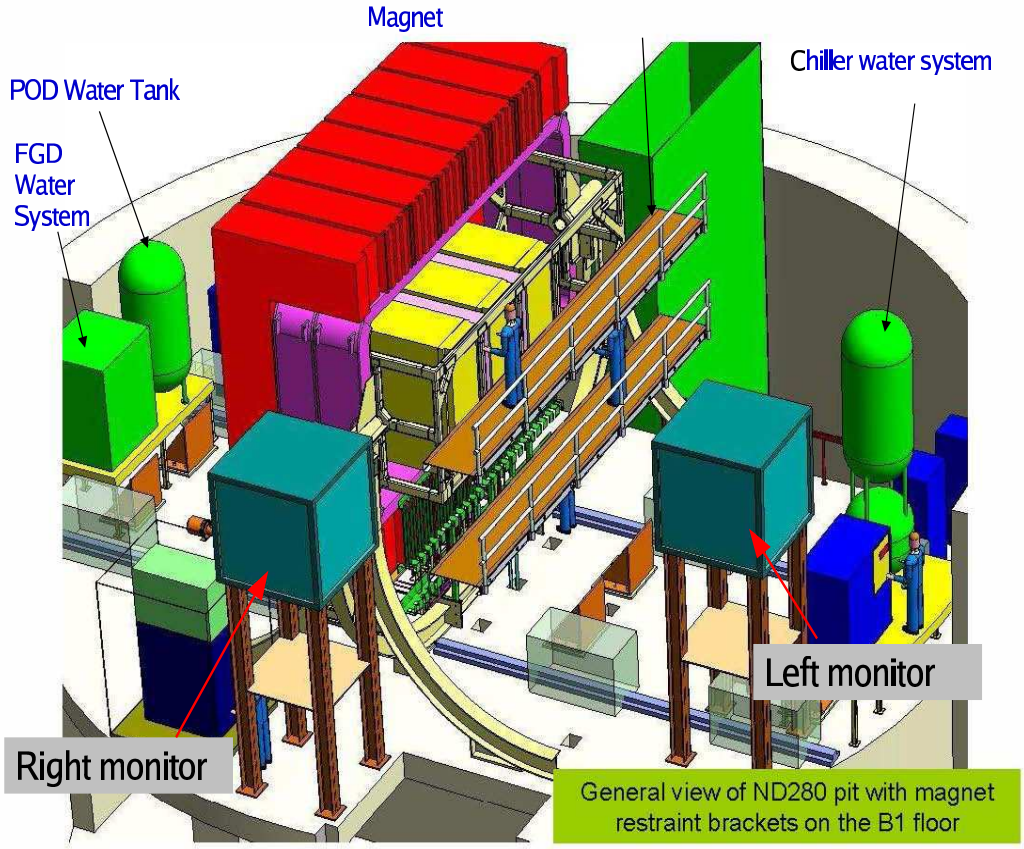

Figure 5: 3D view of the 280m hall detector [2].

2 The design of the Left-Right monitor detector

The task of the Left-Right (LR) monitor is to detect neutrino interactions inside the detector using two identical modules. Since the monitors will be located off-axis with respect to the beam direction the beam energy range is lower than that of the INGRID detector. Therefore, the proposed detector uses iron and scintillator planes, both 1 cm thick. This will allow measurement of lower momentum muons from CC events in the region around 300 MeV/c. The detector size is limited due to the available space in the 280m hall (2×2 m^2 for each module). In addition, both modules should be identical in order to minimize systematic uncertainties. They should be also easily swappable to further reduce these errors.

One module consists of 50 square iron plates, each followed by a square scintillator plane. The detector is surrounded by veto scintillator planes. Both counting and veto scintillator planes consist of 20 scintillator bars equipped with wave length shifting (WLS) fibers. The WLS fiber is held by one sleeve and at one end it is connected to an optical fiber to feed light to a Hamamatsu 64 channel multianode PMT. The iron plates and scintillator planes are installed in a folder from the top of the module. Each module is placed

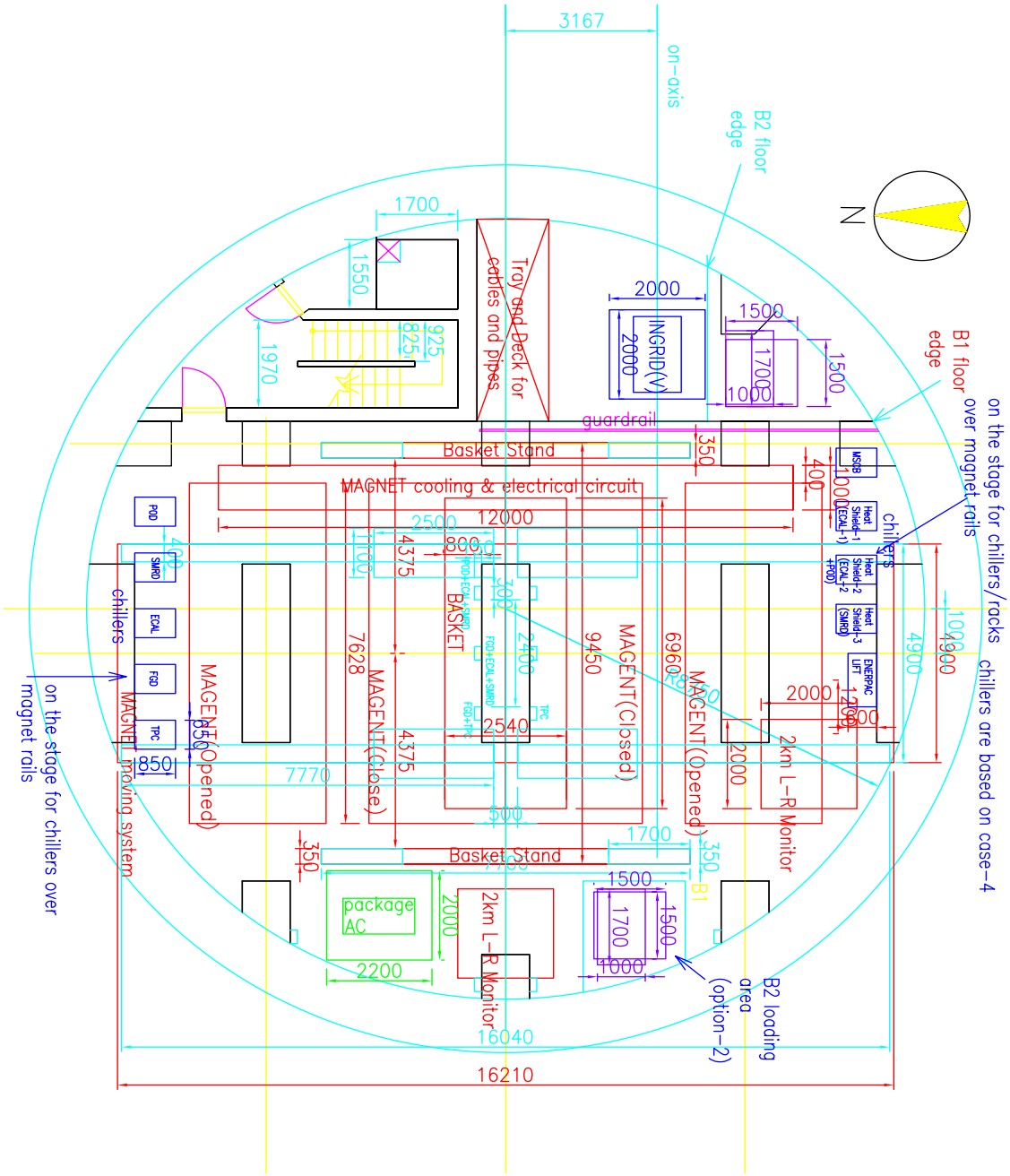

Figure 6: Top view of the 280m detector hall. The neutrino beam enters from the top of this drawing. The two locations for the Left-Right modules are at 2.5 degrees off-axis from the beam direction: the right module placed 6.32 m downstream of the center of the magnet, points directly to Super-K, while the left module placed 2.5 m downstream of the magnet, points directly to the 2KM detector with the same off-axis angle.

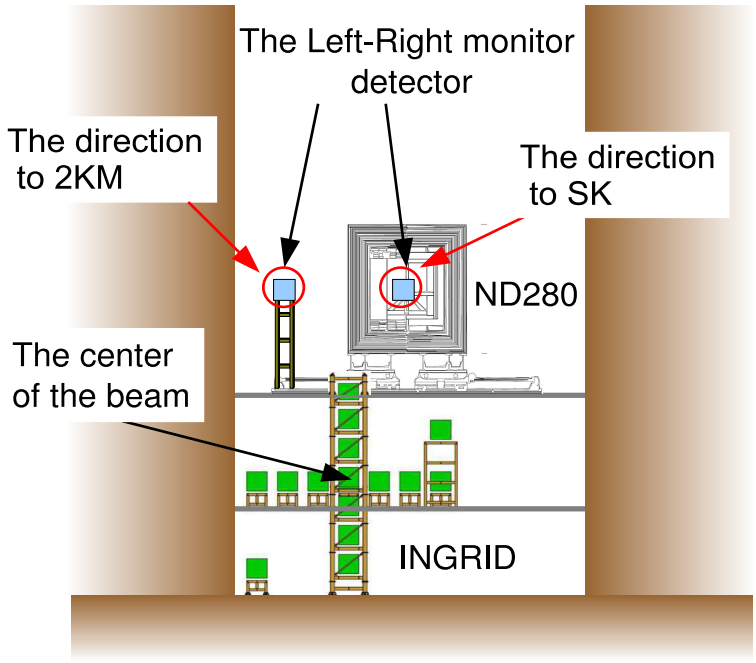

Figure 7: Transverse view of the 280m detector hall. The Right module will be placed behind the magnet, along its longitudinal axis.

on a stand which is about 4 m height in the ND280 hall.

The proposed DAQ system has proven performed reliably during its use in the OPERA experiment, and the expertise gained so far will facilitate easy operation for the LR monitor. In addition, the Hamamatsu multianode PMT is known to have a low dark rate (10 Hz per pixel), so there will be no need to cool the system. Since only a few cables are connected to the readout system, it will be possible to swap the modules and perform comparison runs. This can be used cancel out possible inter-calibration errors. A drawing of one module of the Left-Right monitor is shown in Figure 8.

2.1 Scintillators and fibers

As we mentioned previously, 50 scintillator planes are installed followed by iron plates. A scintillator plane has a dimension of 1×1 m^2 with 1 cm thickness. Each scintillator plane consists of 20 scintillator bars with a size of 100×5 cm^2 and 1 cm thick. Figure 9 shows the engineering drawing of the scintillator produced at Fermilab. The scintillator planes are placed in horizontal and vertical directions alternately according to the beam direction.

In addition, six scintillation planes are installed upstream of the detector in order to calibrate the tracking efficiency in low density material. We expect 1.3 % of the events will interact in these upstream scintillators. This corresponds to about 100 events per year. The analysis of these events will be discussed

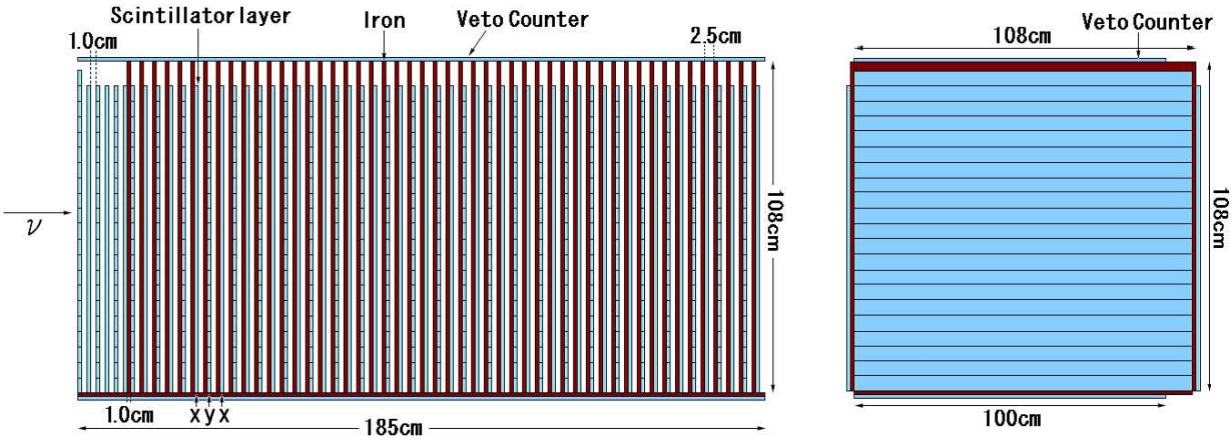

Figure 8: Schematic drawing of the Left-Right monitor module (side and top view). The scintillator layers are displayed in blue and the iron plates in brown. The T2K neutrino beam comes from the left-hand side.

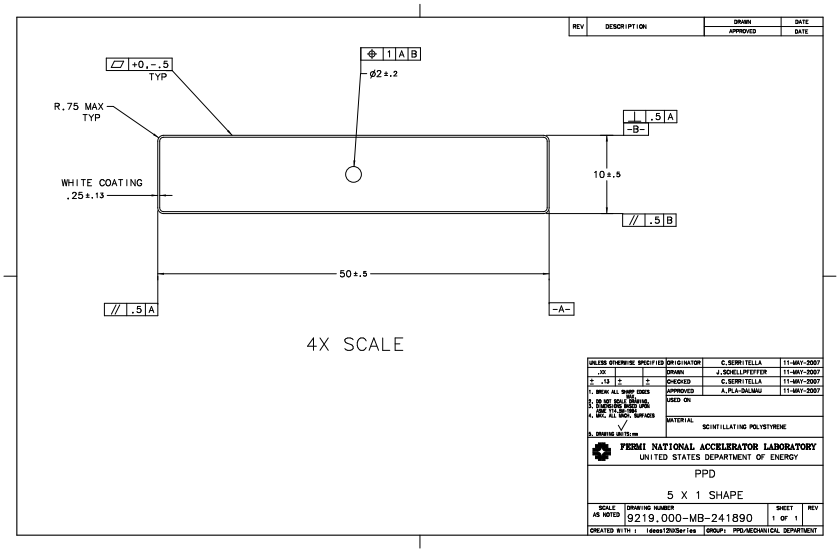

Figure 9: An engineering drawing of the cross-section of the scintillator produced at Fermilab.

in Section 3.6.

The up-most and down-most scintillator planes are used as veto counters in order to select events contained inside the detector volume. We plan to build four 100×185 cm^2 scintillator planes with 100×5 cm^2 scintillator bars as acting veto on the top, bottom and sides. A summary of the scintillator bar dimensions is listed in table 1. Each scintillator bar has a groove in the center for the 1 mm diameter Kuraray Y-

Table 1: Summary of the Left-Right monitor specification for one module.

part	size	number
counter plane	$100 \times 5 \times 1$ cm^3	1080
veto plane (up/down stream)	$100 \times 5 \times 1$ cm^3	40
veto plane (top, bottom, sides)	$100 \times 5 \times 1$ cm^3	148

11(200) WLS fiber used for light collection. The fiber is held by a sleeve at one end with optical couplings via a Kuraray clear-PSM multi-cladding optical fiber to feed the light to the photo multiplier.

2.2 Optical connections

The first optical connection is between the scintillating fibers and the clear fibers. This is realized by means of a brass optical connector. Then, 20 fibers from one counter plane are collected with a single plastic piece. Subsequently, an intermediate optical collector pulls together the fiber bundles from three counter planes and connects the fibers to a single collector that optically couples to the PMT.

Figure 10 (top) shows the details of the optical connection between the scintillating and the clear fibers. Close to the plastic scintillator a sleeve is glued to the scintillator to hold the WLS fiber. In figure 10 (top) we see the cylindrical component that holds the clear fiber, matching the two fibers with a precision of ~ 100 μm. We also see what the connector looks like after mounting. Both sides of the fibers are polished together with their sleeves.

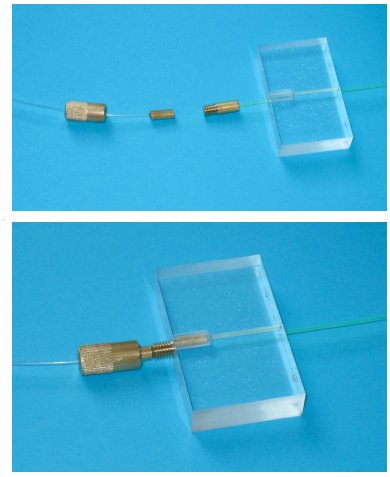

Figure 10: The brass optical device connecting WLS and clear fibers.

The clear fiber has no rubber cladding and is light-tight due to a black plastic pipe that protects the fibers up to an optical collector called "cookie" (figure 11) that keeps the full bundle of 20 fibers from one counter plane together. The cookie also has a rectangular groove on one side in order to facilitate the gluing of the pipe protecting the fiber bundle.

Figure 11 is a drawing of the cookies. The same type of cookie is also used to precisely position each fiber in front of its PMT channel: a total of 60 fibers from three counter planes.

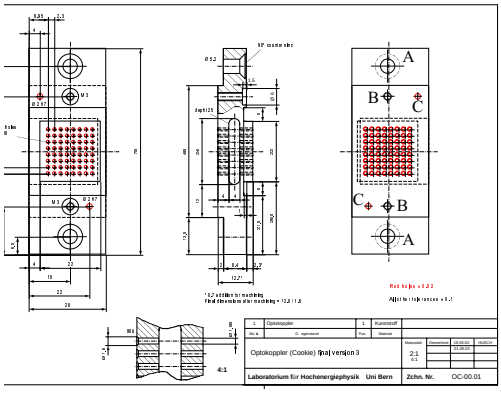

Figure 11: Optical coupling piece (cookie).

The cookies are of two different types: those that connect the fibers of one plane to the intermediate collector and those that connect the intermediate connector to the PMT. The two types of cookies have 20 and 60 holes, respectively, of 1.08 mm diameter to receive the free ends of the fibers. They are equipped with a pocket that is potted with molding Araldite glue to form an optical window after machining.

Several other holes are present on the cookies. Holes B and C (figure 11) are used to fix and precisely align the cookies with the intermediate collector and with the PMTs.

All cookies are made with the same technique and the fibers are mounted on the cookies in the same way: glued and machined with cookie. All fibers are polished together with the collectors and are matched to a precision of ~ 100 μm. Such precision affects the light yield collection at $< 10\,\%$.

The intermediate fiber collector shown in figure 12 is installed on the same board where the electronic readout chain and PMT is mounted. It fits three cookies holding 20 fibers each into the single cookie holding the 60 fibers that are precisely matched to the PMT photocathode channels. The optical connection between the three bundles of 20 fibers and the single bundle of 60 fibers is made by clear fibers placed in the intermediate collector.

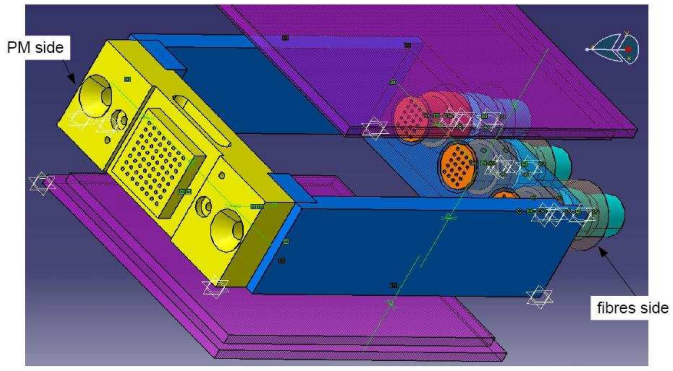

Figure 12: Intermediate light collector.

Table 2 lists the total number of optical elements.

2.3 PMTs

The readout of the Left-Right monitor modules by Hamamatsu M64 multianode photomultipliers coupled to the OPERA DAQ system represents an "off the shelf" fast, stable and reliable solution. The idea is to

Table 2: Number of optical components and connectors.

brass connectors	1280 (3840) components
cookies per plane (20 fibers each)	$56 + 8$ (veto)
cookies per PMT	22
intermediate collectors	22

maximize operational stability and the possibility of swapping the two modules to reduce intercalibration errors, while minimizing the construction effort:

- the M64 have a very low dark count rate (10 Hz per pixel) and do not need to be thermalized. The response is equalized, uniform and stable over time
- the application of this system to the OPERA experiment featured stable and rubust continuous operation for more than two years
- each module is connected to only a few Ethernet cables (for data and clock distribution) and a low voltage cable. High voltages are generated locally
- all the necessary electronics and software are already available. There is good expertise in the Lyon and Bern groups, who contributed to the implementation of this system in OPERA. The software is already structured for remote control and has been tested in OPERA for two years. The output data format is in the form of ROOT n-tuples and is completely compatible with those of the INGRID data.

The choice of photodetector is based on considerating the single photoelectron efficiency, quantum efficiency in the WLS fiber emission spectrum, low dark count rate, low cross-talk, lifetime and cost. The proposal to use the commercially available 64-channel Hamamatsu H7546 PMT as it was modified for OPERA is motivated by the large expertise gathered with that device not only in OPERA but also in the MINOS experiment where it instruments the near detector scintillator tracker. A picture of the PMT and the "cookie" to which it is attached for the fiber-to-pixel connections is shown in figure 13.

Figure 13: H8804MOD-1 PMT with alignment pins and cookie.

The characteristics of this PMT provided by Hamamatsu are given in table 3.

The modifications requested for the OPERA Target Tracker were focused on geometrical specifications in order to:

- achieve better alignment between the fibers and the PMT pixels by requesting a better positioning of the PMT inside its plastic housing. This was done by adding some black high voltage proof resin between the PMT and the plastic housing;
- fix the PMT on the alignment "cookie" by adding two extra "ears" to the original rectangular plastic housing;

Table 3: Characteristics of the 64-channel Hamamatsu H7546 PMT.

photocathode material	bialkali
window material	borosilicate
spectral response	300-650 nm
wavelength of maximum response	420 nm
number of dynode stages	12
anode size	2×2 mm^2
maximum supply voltage between anode and cathode	1000 V
divider circuit	$3:2:2:1:\cdots:1:2:5$
divider current at 1 kV	455 μA
gain at 800 V	3.0×10^5
cross talk (with 1 mm optical fiber)	2 %
uniformity among all anodes	1:3

- improve the light-tightness from the back plane (thanks to the black resin).

Figure 14 shows the H8804MOD-1 PMT layout and resistor divider as they are provided by Hamamatsu. Each channel consists of by two sets of 12 dynodes and each cell covers an area of 2.3×2.3 mm^2 (figure 15). The PMT also provides the output from the last dynode, number 12.

Expected PMT performance By pulsing a LED and recording events in correlation with the input signal one gets the spectrum displayed in figure 16 for a typical voltage of 800 V. The response of a single channel is parametrized by the convolution of a Poisson and a Gaussian distribution:

$$\begin{aligned} S &= P_\mu(n) \otimes Gauss_{Q,\sigma} \quad \text{where} \\ P_\mu(n) &= \frac{\mu^n}{n!} e^{-\mu} \\ Gauss_{Q,\sigma} &= \frac{1}{\sigma\sqrt{2\pi}} e^{\frac{-(q-Q)^2}{2\sigma^2}} \end{aligned}$$

This distribution function is used to fit an PMT's response. Two different Gaussian parameter sets are used for the pedestal on one side, Q_0 and σ_0, and for the p.e. peaks on the other side, Q and σ. The single p.e. gain is given by Q. The other parameters are the mean number of p.e., μ, and the overall normalization constant, A. The best procedure to reliably fit the PMT response is to perform a separate fit of the pedestals (with a null light level from the LED or a random trigger) and then run with a reasonably low light level (μ ranging from 1 to 4) in order to limit the statistical weight of the pedestal region where different phenomena are to be taken into account in the procedure:

- intermediate peaks between the pedestal and the single p.e. peak (direct photo-conversion on the first dynode stage)
- double peak structure due to the different response of the 2 dynode system of an individual channel (see figure 15)
- "exponential" response in the pedestal tails.

All of these phenomena lead to strong uncertainties in the gain determination and should be avoided.

The gain spread between individual channels can range from 1 to 3. The readout electronics used here provide a correction to this drawback (see Section 2.6.1). After correction, the gain uniformity has the distribution shown in figure 17. The ratio σ/average in this case is around 6 %.

As far as the absolute gain of each channel is concerned one can set the high-voltage in a way that the gain of the strongest channel of each PMT equals 10^6. The gains of the 64 channels are electronically

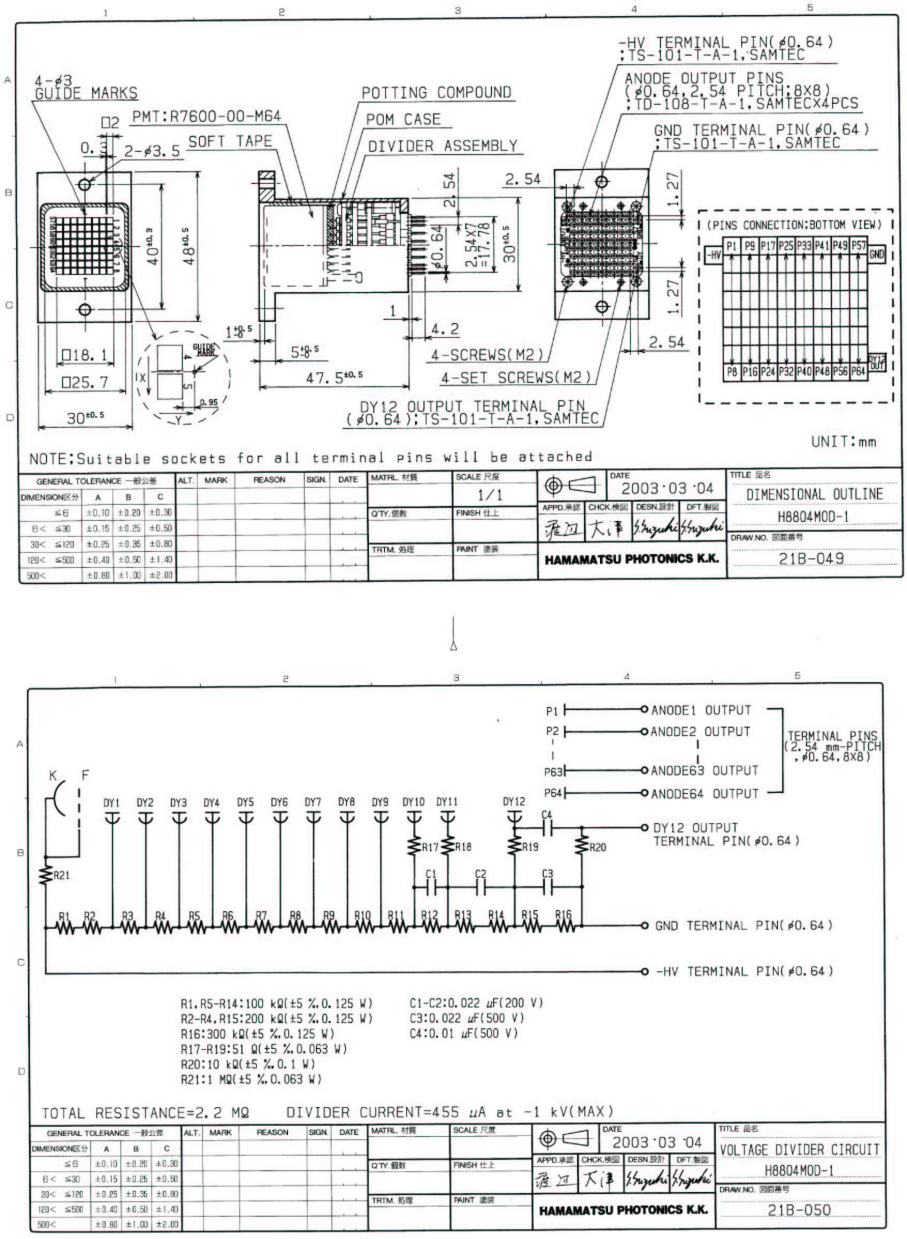

Figure 14: H8804MOD-1 multianode PMT layout (top) and resistor divider (bottom).

equalized by means of the front end chips. The gain variation without the high voltage value follows a power law: $G(HV) = G(HV0) \times (HV/HV0)^{\beta}$, where $\beta \simeq 10$.

The counting rate induced by natural radioactivity or PMT dark current must be as low as possible to reduce the effect of dead time. Using the Hamamatsu 64–channel PMT with a threshold corresponding to 1/3 p.e., a noise less than 10 Hz at 25 ^{o}C has been measured coming from photocathode thermoemission. This possibility of using a low threshold assures a high single p.e detection efficiency and considerably reduces the effect of gain dispersion between PMT channels.

Fifty PMTs will be systematically tested on a dedicated test bench using the same electronics as for the final readout. A picture of the active components of that test bench is displayed in figure 24. The full electronic chain is calibrated by injecting charge signals directly into the front-end chips to measure the

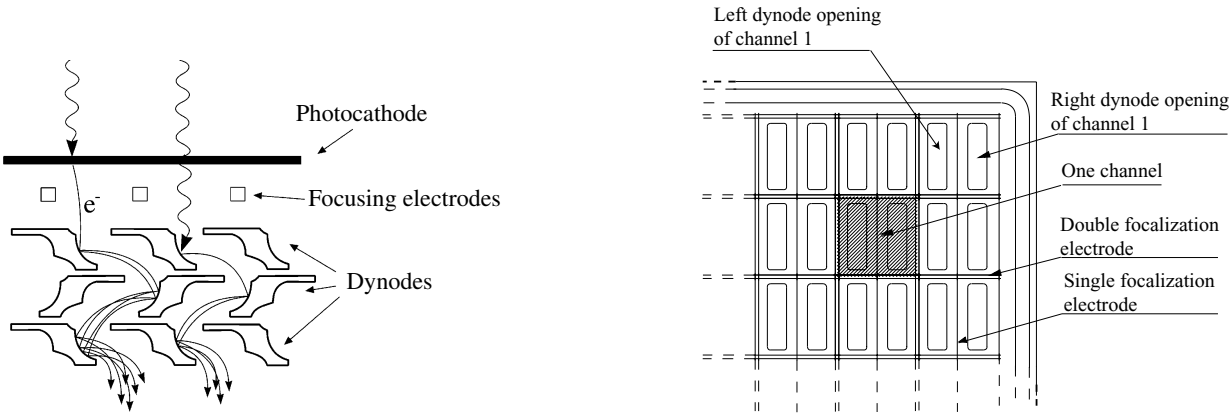

Figure 15: Schematic view of the multiplication process inside a multianode PMT (left) and of the channel separation by focusing electrodes (right).

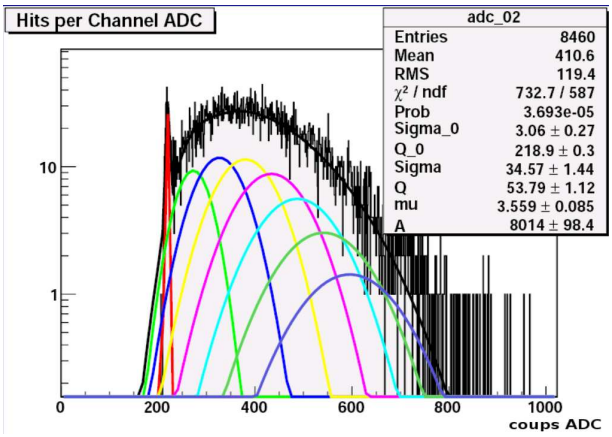

Figure 16: Typical spectrum of a PMT channel. The mean number of p.e. is above 3.5.

absolute gain of each of the 64 channels and also by comparison with a reference PMT. The LED pulsing system includes two LEDs flashing on each side of a diffuser in contact with the PMT input window. The surface of the diffuser is larger than the PMT's window to limit edge effects. PMTs are screwed on the metallic bar holding the LEDs and the diffuser. The position of the PMTs input window is reasonably accurate in this configuration thanks to the modified geometry of the PMT plastic housing.

The test sequence has the following steps:

1. **Pedestal measurement**: measure the pedestals with high voltage OFF then with a typical high voltage of 800 V.

2. **Pre-test**: Find the high-voltage (HV0) where the gain of the strongest channel equals 10^6.

3. **Absolute gain calibration**: using an average light level of 2.5 p.e. and the fitting model described above. All 64 channels are illuminated in one run. Some 100k events are then used to perform the fit.

4. **High-voltage curve**: runs at $\simeq$15 p.e. will be taken in a $\pm$ 30 V range to determine the HV curve for each channel.

5. **Linearity**: The PMT linearity is checked by varying the LED amplitude.

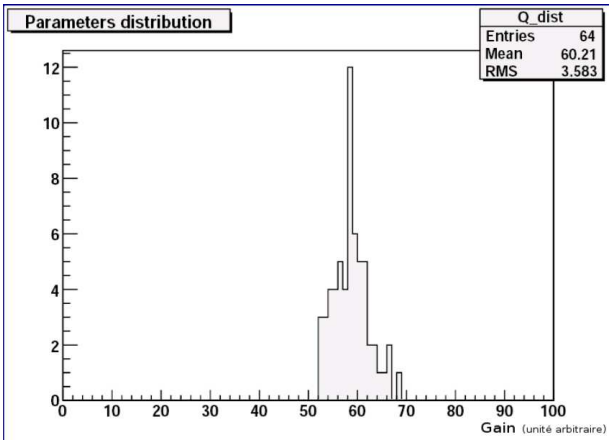

Figure 17: Typical gain distribution over the PMT 64 channels.

6. **Dark-current**: Events are acquired during 20 seconds, triggering on each individual channels with a threshold set at 1/3 p.e.

A full test takes less than one hour. All relevant results are stored in a database.

2.4 Mechanical structure of the modules

The two modules constituting the Left-Right monitor have the same design (see figure 5). Each module has 50 iron plates and 56 counter planes where 51 out of the 56 are alternated with the iron plates and 5 are positioned in the upstream side of the module without iron plates in between. All counter planes are identical, while the iron plates differ in size as seen in figure 18. The horizontal top bars, which can be

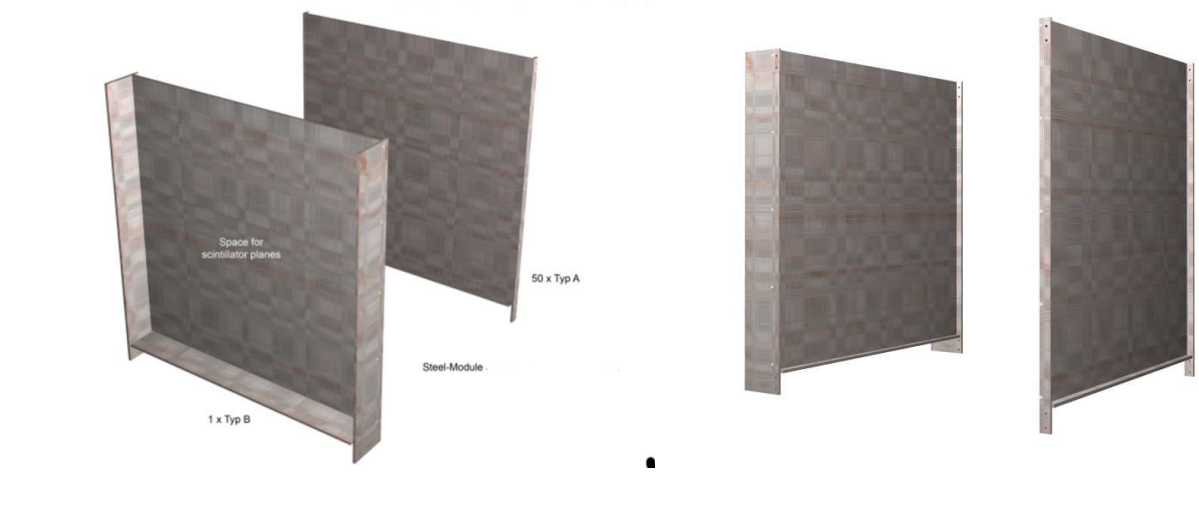

Figure 18: Several types of iron plates with different kinds of wings.

seen in figure 19 (right), support the veto counter. The veto system is made of two counter planes for each side of the module. Similarly, the two bottom veto planes are supported by the same types of bars, but the counters are installed in the space in between the bottom of the iron plates and bars. All the bars and the four rings are screwed to the main support beams. There are four rings allowing the full module to

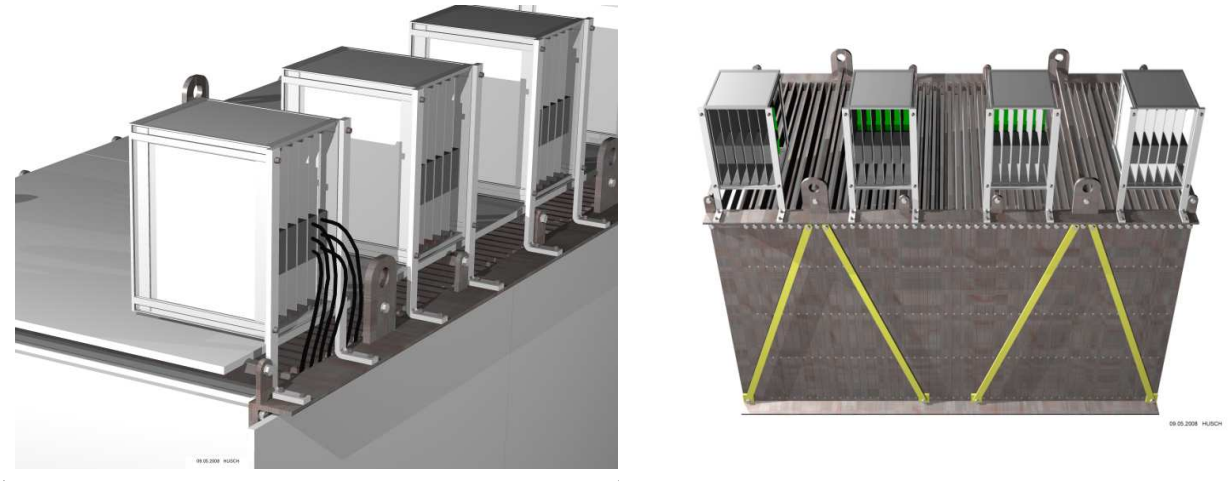

Figure 19: A module with readout boxes mounted on the top. Veto counters are also shown in the left picture.

lift off and be replaced it. For the left and right veto counters (two planes on each side), two "L" shaped support beams are used to support the counters that are fixed by stoppers.

The last component of the mechanical structure is the box (4 "crates") where the 17 electronic boards with the readout electronics and a PMT are installed. The crates are fastened by means of feet to the right support beam, as seen in figure 19. One fully assembled module with veto planes and readout boxes is shown in figure 20.

Each iron plate has a squared surface of 1080×1080 mm^2 and a thickness of 10 mm. They are fitted with two small wings whose dimensions are $1080 \times 20 \times 10$ mm^3. The wings are fastened by 5 screws to the left, right and bottom edges of each iron plate (figure 18). The iron plate structure is able to host and support the counter planes. Soft foam or a plastic spring is used to fix the counter planes in place.

The counter planes are inserted into an aluminum box whose dimensions are $1060 \times 1015 \times 15$ mm^3 (figure 21, top) and contain 20 scintillator bars. Only the most upstream plane is made of 21 bars with 108 cm long scintillator bars in order to instrument the corner. Otherwise, this corner would be a dead zone for particle detection. Moreover this provides better background rejection (see Section 3.4). The choice of the first plane with one more scintillator bar also requires the use of special cookies, two with 21 holes and one with 61 holes.

Each counter plane has a multi-layer structure. It consists of a 1 mm thick aluminum sheet 1060×1015 mm^2 in surface area, double sided scotch strips, a series of 20 scintillator bars, again double sided scotch strips on the scintillator bars and finally one more aluminum sheet to close the counter plane structure. The double sided scotch strips and the aluminum sheet provide the counter plane with the desired mechanical rigidity. Figure 21 shows the multi-layer structure of the counter plane. One of the two aluminum sheets is equipped with small wings (top/bottom) of $1060 \times 12 \times 10$ mm^3 attached with epoxy. The other sheet also has left and right wings obtained by bending the edges of the full sheet. In figure 21 one can see that the top aluminum sheet has a smaller size ($960 \times 1015 \times 15$ mm^3) than the one at the bottom of the counter plane.

After the counter plane is assembled the fibers from the 20 scintillator bars are inserted into a black pipe that is glued to the cover and to the cookie. Table 4 shows the construction parameters of each module.

2.5 Mounting procedure

The mounting procedure starts with the two different types of planes (A,B) with all wings ready to be assembled. The iron plates are screwed one by one to the four supporting beams. When the iron structure is assembled, the counter planes are installed from the top of the monitor into the space between the iron plates. The counter plane is lifted by a crane thanks to four flat ropes glued to the aluminum sheets.

Figure 20: One of the two modules fully assembled with veto planes and readout boxes.

Table 4: List of the mechanical components of one module.

elements	number	size
iron plates type A	40	$1080 \times 1080 \times 10$ mm^3
iron plates type B	4	$1080 \times 1080 \times 10$ mm^3
left, right and bottom wings	150	$1080 \times 20 \times 10$ mm^3
support beam	4	L shaped 1920 mm length
counter planes	$51 + 5$	$1060 \times 1015 \times 12$ mm^3
veto-counter planes	8	$1060 \times 1015 \times 12$ mm^3

Subsequently, the veto counters are installed: top/bottom and left/right. After that the crate hosting the readout boards is fastened to the support beam. The cookies from the different planes are pulled together three by three and connected to the intermediate collectors installed on the boards where also the readout electronic is mounted.

Each module is positioned on a ~ 4 m high stand which is made of two main parts kept together by 60 screws ($M20$) as shown in figure 22. The main support beams of the stand are made of four empty lateral pillars with a square cross-section of 200×200 mm^2 and 10 mm thickness. The two components of the stand are reinforced by means of two bars per side and then cross mounted to prevent oscillations in the event of an earthquake. The dimensions of the bars are 100×100 mm^3.

Figrue 22 shows the detector module fully assembled with its stand. The bottom part of the stand is slightly different from the top part. Two feet ($200 \times 200 \times 10$ mm^3) are used to fasten the full structure (stand + detector) to the pit floor with $12 + 12$ screws ($M30$). The weight of the stand is almost 4.9 tons. Therefore the crane has to handle module and stand separately. As seen in figure 23 the stand base is equipped with two feet and two open sides. This allows the magnet rails and other pipes or cables to pass through the space between the feet.

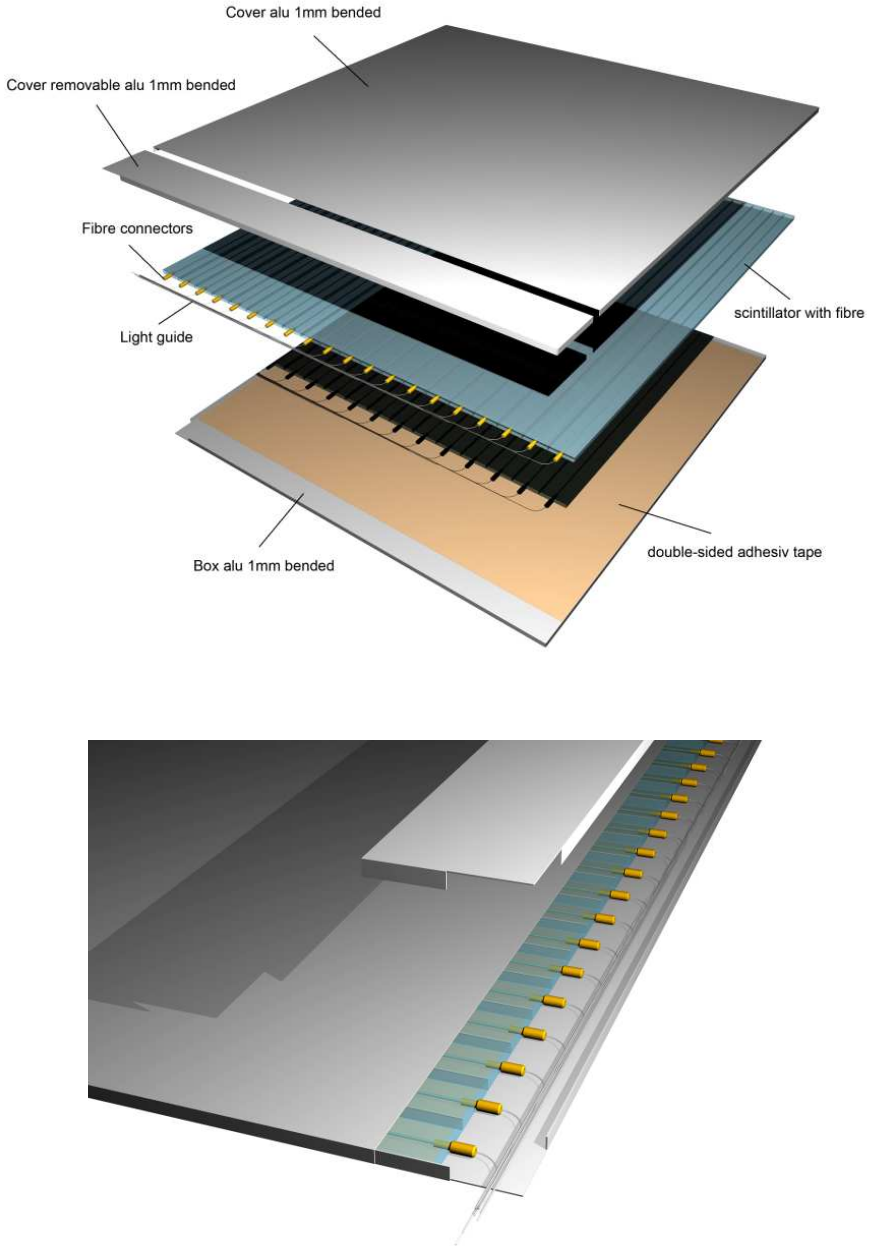

Figure 21: Details of the counter plane structure.

Figure 22: Picture of one module fully assembled with its 4 m high stand.

Figure 23: Details of the stand feet (left) and of the clamping system of the detector to the stand (right).

2.6 Readout electronics

This section describes the complete electronics chain used to readout the Hamamatsu M64 PMTs. This readout electronics chain has been developed for the OPERA experiment and has been tested and validated using 992 PMTs. It has been continuously running for two years in a stable and reliable way. It is based on the concept of Ethernet capable smart sensors where data are acquired asynchronously, time-stamped and transmitted through a standard network to an event builder PC. This PC is offline and takes care of data sorting and time matching of hits belonging to the same time window with 10 ns accuracy. Each sensor (M64) is connected to two different electronics boards:

- an analog front-end board directly plugged to the PMT housing two 32-channel ASICs
- a digital motherboard including fast ADC, a high voltage module, a LED pulse generator, a clock decoding unit and a micro-processor daughterboard called "mezzanine" connected to the rest of the system via a standard Ethernet link.

The full PMT readout chain is displayed in figure 24.

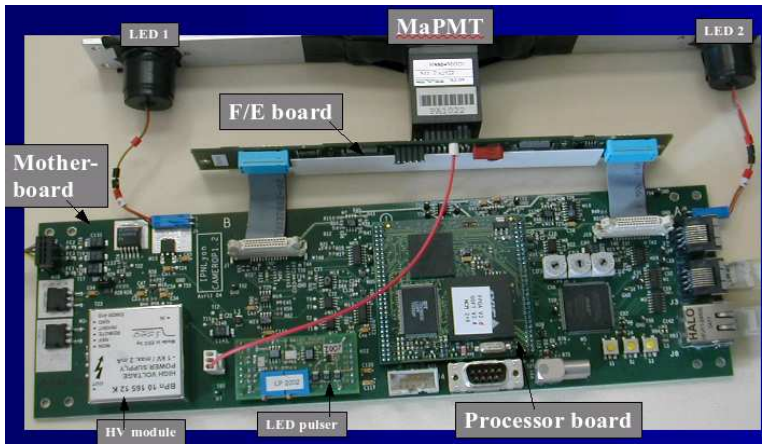

Figure 24: Picture of the complete PMT readout chain.

The main features of the analog and digital readout electronics, DAQ and event building system are:

- triggerless operation mode (to allow continuous recording of events)
- accurate timestamping locked on the GPS (to correlate off line events)
- continuous running capability
- low deadtime
- modular and flexible hardware/software architecture (trigger schemes, on line and off line filters etc).

The Ethernet capability makes the readout chain very compact and minimizes the cabling. Each Left-Right module can be connected to the PC which will act as event builder with one Ethernet cable, one clock cable and the low voltage cables. High voltages are generated locally on the cards. A network switch located on the module itself will interconnect the various cards. The module can be thus unplugged and moved very quickly and easily. All the software and graphical user interfaces for the control of the DAQ system, including remote WAN control and ROOT output, already exist and are well tested. The data can be written by the event building PC in the same ROOT ntuple format as for the INGRID detector.

2.6.1 Front-end electronics

The 32-channel ASIC used to readout the PMTs signals has been designed at LAL (IN2P3-CNRS, France) and called OPERA-ROC (OPERA Read Out Chip). A detailed description of the ASIC design and performance can be found in [4, 5, 6]. All quantitative statements refer to a nominal PMT gain of 10^6 (1 p.e. = 160 fC). The main features of the chip are the following:

- PMT anode gain spread correction (within a minimal dynamic range of 1:3);
- auto-triggering capability with a 100 % trigger efficiency at 1/3 p.e.;
- 100 p.e. dynamic range for the charge measurement (signals up to 16 pC).

The ROC is a 32-channel ASIC. The global architecture of a single channel is displayed in figure 25.

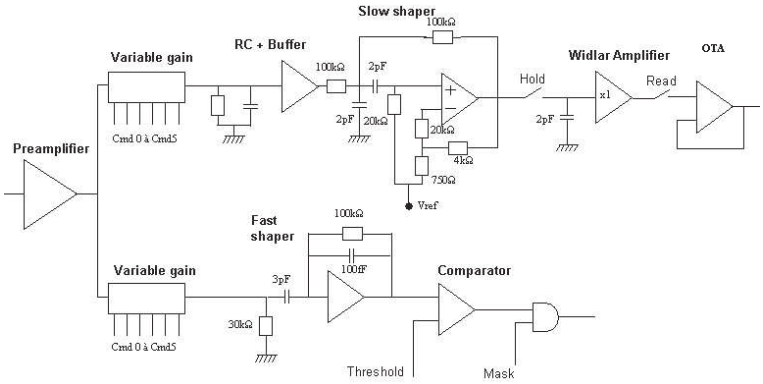

Figure 25: Architecture of a single electronic channel.

The first stage of an individual input is a preamplifier with adjustable gain through two independent current mirror structures (2, 1, 0.5, 0.25, 0.125, 0.0625) set externally. The activation of the six switches thus allows effective gain correction ranging from 0 to 3.9. Each channel can be also de-activated by turning off all of its current switches. The preamplifier gain is 94 mV/pC (15 mV/p.e.) with a rise time of about 30 ns, for a correction gain set to 1. The noise RMS is below 1 % p.e.

After the preamplifier two copies of the input current feed a two-shaper stage:

- A fast shaper (fed via a 3 pF capacitance and integrated in a 0.1 pF charge amplifier for a resulting peaking time around 10 ns) followed by a discriminator whose threshold is common for the 32 input channels. The trigger is defined as the logical "OR" of the 32 channels. A mask register allows any particular channel to be enabled/disabled from the trigger scheme. Trigger efficiency is 100 % at 1/10 of p.e. (figure 26).
- A low-noise slow shaper (Sallen-Key shaper characterized by a time constant of 200 ns) for the charge measurement. Pedestal variation dispersion is minimized by the use of a differential input stage. The slow shaper is followed by a Track and Hold buffer and multiplexed output. The buffer allows the charge signal to be stored at its maximal value in a 2 pF capacitor for readout. The delay between the trigger and the *hold* signal is adjustable in order to optimize the precision of the charge measurement but also allows the use of an external trigger with a different timing scheme. Charge signals are afterwords multiplexed at 5 MHz and are available for sequential readout through a shift register. The linearity is better than 2 % over the full range 1-16 pC for a preamplifier gain of 1, corresponding to 1-100 p.e.

The performance of the preamplifier and shaper stages are summarized in table 5. The technology of the chip is AMS BiCMOS 0.8 μm. The chip area is about 10 mm^2 and it is packaged in a QFP100 case. The chip consumption depends upon the gain correction settings and ranges between 130 mW and 160 mW (32 channels).

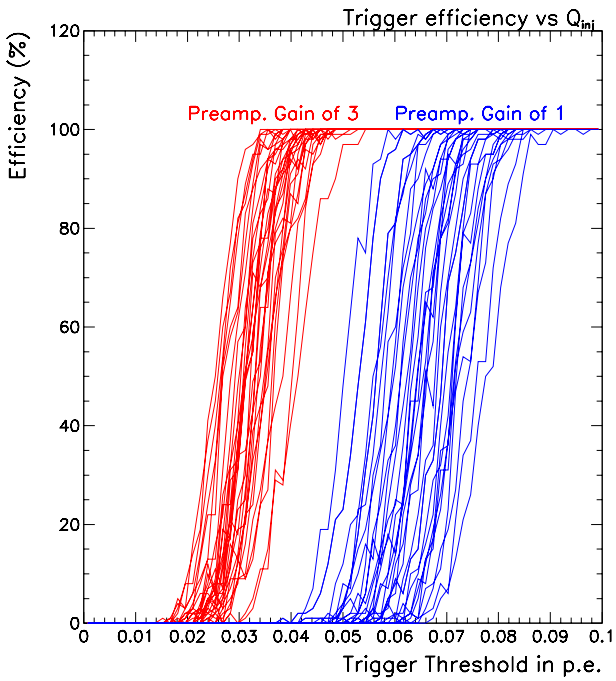

Figure 26: Trigger efficiency (S-curve) as function of the input charge for the 32 channels for a preamplifier gains of 1 and 3.

The front-end chips are mounted on an 8-layer PCB plugged just behind the PMT. The width of the PCB has been designed so as not to exceed the width of the PMT (3.4 cm). The board is connected to the DAQ motherboard through two flat cables (1 per chip typically) while a dedicated high voltage cable brings the HV from the motherboard to the PMT. A 20 MΩ resistor allows a direct measurement of the applied HV for monitoring.

2.6.2 DAQ architecture

The central elements of the DAQ system are the Ethernet Controller Mezzanine (ECM) boards including a micro-processor (ETRAX 100LX from AXIS), a sequencer (ALTERA FPGA of the "cyclone" family)and an intermediate buffer (IDT FIFO).

The mezzanine has 120 pins divided in 4 rows. 60 I/O are available for the readout or slow control. These signals are directly connected to the FPGA and can be reconfigured. A second group of signals is dedicated to system management: power supply, Ethernet link, RS232 debug link, external reset, Flash Load control and JTAG FPGA configuration. A third group of signals is also required for the interface with the clock distribution system: reference clock time stamp, PPS increment, PPS reset and time control serial link. The physical view and a block diagram of the ECM is shown in figure 27.

The sequencer The FPGA firmware allows the following tasks to be performed:

- sequencing of the readout (clocks, R/O registers, digital I/O);
- local data processing (zero suppression, event validation with an external trigger if requested);
- event time stamping (via a local fine counter at 100 MHz synchronized with the global distributed clock);
- data formatting and storage in a FIFO;
- data transfer to the external FIFO;

Table 5: Performance of the OPERA ROC.

PREAMPLIFIER	
- gain correction	range 0-3.5 (6 bit resolution)
	2,1,1/2,1/4,1/8,1/16
- input for test pulse	3 pF alternate (even/odd channels)
- input Impedance	$Z_{in} \approx 100\ \Omega$
AUTO-TRIGGER:	
- fast shaper peak time	10 ns
- fast shaper gain (Gain 1)	2.5 V/pC (400 mV/p.e.)
- threshold spread	0.03 p.e.
- fast shaper noise (Gain 1)	1.8 mV (0.72fC or 0.005 p.e.)
- trigger sensitivity	100 % at 0.1 p.e.
- hit register	implemented
CHARGE MEASUREMENT:	
- dynamic range (Gain 1)	16 pC (100 p.e)
- slow shaper peak time (Gain 1)	160 ns
- slow shaper gain (Gain 1)	120 mV/pC (19 mV/p.e.)
- pedestal spread (mV)	± 6 mV (widlar) / ± 9 mV (CC)
	$(\pm 0.4 - 0.5$ p.e.)
- noise @ MUX rms (Gain 1)	1.3 mV (12 fC or 0.075 p.e.)
- crosstalk	$\mathcal{O}(1\,\%)$
linear voltage range @ MUX	about 2.2 V to 4.2 V
clock frequency	5 MHz (6.4μs/32ch.)

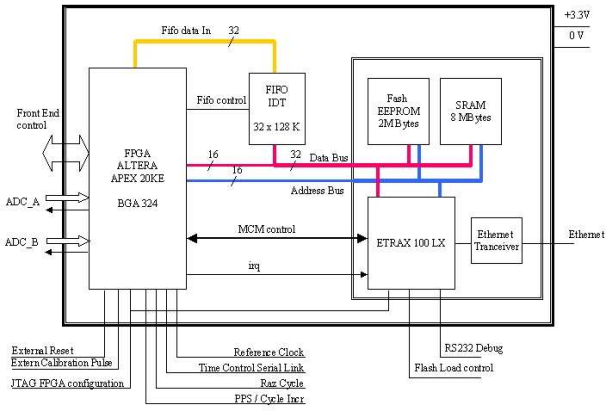

Figure 27: Mezzanine block diagram and physical view.

- slow control;
- interface with the Ethernet processor.

From the DAQ point of view these control and readout sequences are made with Ethernet. The FPGA (and also the external FIFO) are seen as an addressable I/O area. The software upload is made with Ethernet.

The Ethernet processor is an ASIC based on the ETRAX 100LX from AXIS. It is a 32-bit RISC CPU using a Linux 2.4 operating system and an Ethernet interface supporting data transfer rates up to 200 Mbits/s. The chip is embedded in a Multi Chip Module (MCM) which includes in a single chip the ETRAX100lx core plus 4 Mbytes of flash memory, 16 Mbytes of SDRAM, an Ethernet transceiver, RESET circuitry and around 50 passive components. The mandatory components outside of it are a 3.3 V power source and a 20 MHz oscillator. The module estimated power dissipation is around 1.2 W. This MCM is equivalent to a full Linux computer in a compact form.

The MCM has to perform the following tasks:

- data transmission from the FIFO to Ethernet;
- slow control interface (control and configuration commands);
- remote FPGA reconfiguration (e.g. to change some control parameters such as pedestal values for zero suppression, time stamp accuracy);
- remote `reset`/`reboot` via the clock distribution command line (see below);
- local data processing: taking advantage of the available CPU and the SDRAM buffer, we perform monitoring functions by recording individual channels histograms.

The FIFO is 32 bits wide and 128K deep. It allows data buffering. The FIFO is seen by the processor as an external programmable device. The FPGA generates an IRQ signal to the ETRAX to read the FIFO. In normal conditions, the IRQ is generated at each PPS and a status register is read giving the data cycle number a flag indicating if the cycle is complete or not and a field indicating the acquisition mode. The IRQ also can be generated with an adjustable words threshold on the FIFO. The mezzanine is plugged in to the DAQ motherboard which hosts the following generic elements:

- F/E controller unit (interface to the analog board for readout, configuration and monitoring);
- the Ethernet Controller Mezzanine (described above);
- the clock unit (clock decoding and propagation delay measurements);
- the power supply unit including the high voltage module for the PMT.

Figure 28 shows the schematic of a generic controller board (left) and pictures of their real implementations (right).

The F/E controller unit includes all DACs to set the various levels in the analog electronics and the readout ADC (Analog Devices 12 bits 5MHz).

The clock unit functions are performed inside an EPLD. The clock bus is a serial M-LVDS bus chained from one board to the next one. The clock signals are ported on a 20 MHz clock:

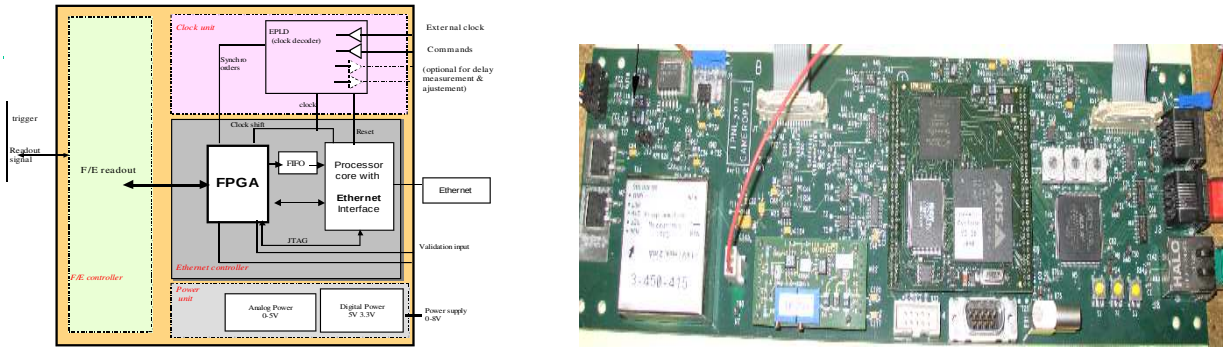

Figure 28: Controller motherboard schematics (left) and a picture (right)

The high voltage module is made by ISEG. The output voltage is in the range 0-1000 V and is DC powered by low voltage DC in the range 0-12 V. The maximal output current is 2 mA. The accuracy of the output voltage is $\pm$ 1 %, the ripple less than 0.01 % peak-to-peak and the temperature coefficient does not exceed $\pm 0.01\,\%/°\mathrm{C}$.

The overall DAQ system includes 48 PMTs (sensors) 24 per module including 4 sensors for the veto planes, for a total of 3072 readout channels. Each sensor is externally seen as a node on the Ethernet network and receives a common clock signal for synchronization of its local clock. The global DAQ network is divided into two parts, a standard Ethernet network and a clock distribution system.

The Ethernet network includes all sensors plus one or potentially two servers for event building, data storage and general services. The network may be divided into various VLANs to separate and secure the data traffic. Each node is connected to a one level 2 100/1000 Mbps 24 port switch which is managed via a level 3 1 Gbps switch acting as the head of the network.

The clock distribution system is a specific link between the Central Clock Unit synchronized on the GPS to each sensor. We require high efficiency for this distribution line. A characteristic feature is the bi-directionality of the system which allows control of the signal reception and the measurement of the propagation time with acknowledge signals. The Central Clock unit is a PCI board which decodes the GPS signal from the external antenna and sends a common 20 MHz clock from a precise oscillator via an optical link. The signal is then converted into electrical format and distributed to the "clock master cards". Each of these cards should deserialize the commands and the clock and distribute both of them to the clock unit of each controller board through another M-LVDS bus. The Clock Receiver unit, which can be addressed either individually or in broadcast mode, receives the control word decodes it and generates a pulse on the appropriate control signal.

2.6.3 Event building and software implementation

Each trigger recorded by a sensor (L0 trigger) is timestamped by latching the value of the local fast counter (100 MHz generated from the common clock via a PLL). This fine time stamp is added to the absolute time of a PPS-like signal generated by the Central Clock unit (a cycle) after correction of the propagation delay: $T_{\mathsf{event}} = T_{\mathsf{UTC}} + T_{\mathsf{fastcounter}}$. All hits recorded during a cycle in the detector are sent by the sensors to the event builder which performs time sorting, searches for coincidences within a sliding and adjustable gate, applies L1 filters and buffers the data before transmission to the Global Manager. The Manager has an overview of all detectors and performs the overall event building after L2 filtering and records the events. The database storage can be either Oracle (version 10g or higher) or PostGres systems.

The distributed client/server software is based on the CORBA standard.CORBA gives each object a reference on a virtual bus (the ORB) so it can be used by any connected application which gets this reference. All entities are connected to the network register using a Naming Service.

The online software connects applications and classifies them into three categories: sensor (L0), sub-detector DAQ (L1) or Manager (L2). The last two offer a G.U.I. designed in the GTKmm framework

which offers the generic methods: `start/stop run`, `start/stop calibration`, `get Sensors connected` and `get parameters`.

2.7 Calibration systems

2.7.1 Scintillator calibration

A method used in the calibration of the scintillator strips of the OPERA target tracker consisted of irradiating them with 1.8 MeV electrons selected with a magnetic spectrometer. The spectrometer contains a commercial ^{90}Sr source shielded in tungsten housing with a collimator. An electron beam is then sent through a vacuum chamber immersed in a magnetic field generated by a coil and then extracted through a pin-hole window which allows for the momentum selection. The device is calibrated to feed the correct DC current. The magnetic spectrometer is shown in figure 29.

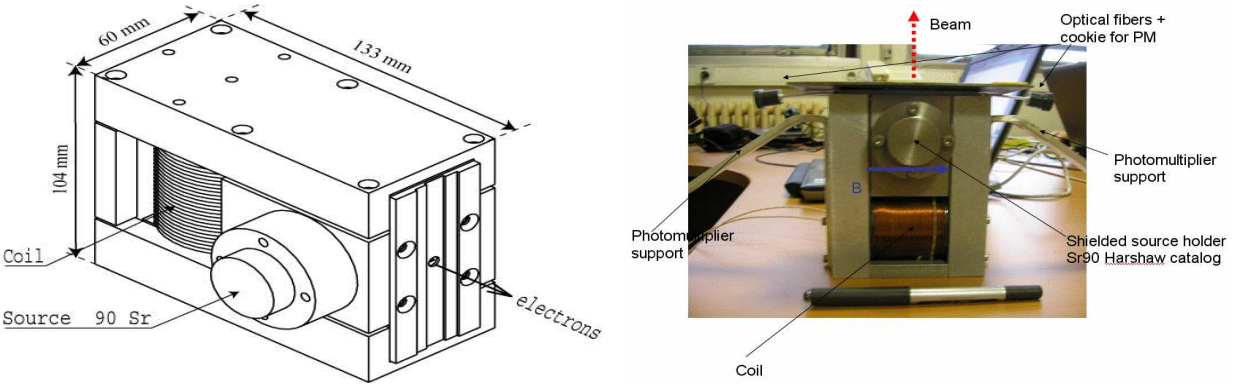

Figure 29: Electron spectrometer: schematics and picture.

A trigger is provided by the coincidence of two 100 micron thick scintillators located after the beam exit window and readout by two photomultipliers. The final rate at 1.8 MeV is on the order of a few tens of Hertz. The spectrometer produces electrons at the ionization minimum. Nevertheless, the path of the electrons is perturbed by multiple scattering as observed in the GEANT simulation shown in figure 30. This broadening effect determines some signal losses when irradiating close to the edge of the scintillator

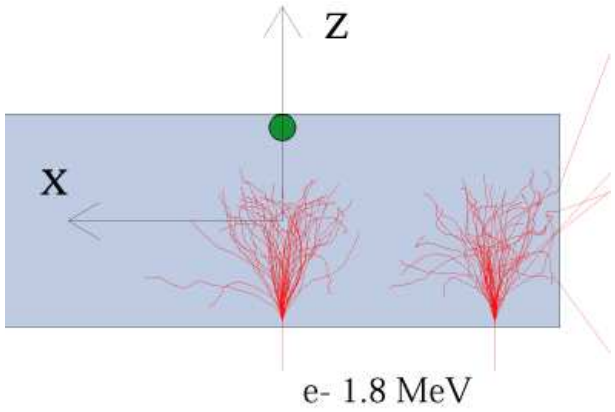

Figure 30: Geant simulation of 1.8 MeV electrons irradiating 1 cm thick and 2.6 cm wide scintillator strip.

strips (figure 31). The calibration of the electron spectrometer signal versus the muon one crossing at the center of the strip was verified on the same scintillator strips in dedicated test-beams at CERN and it

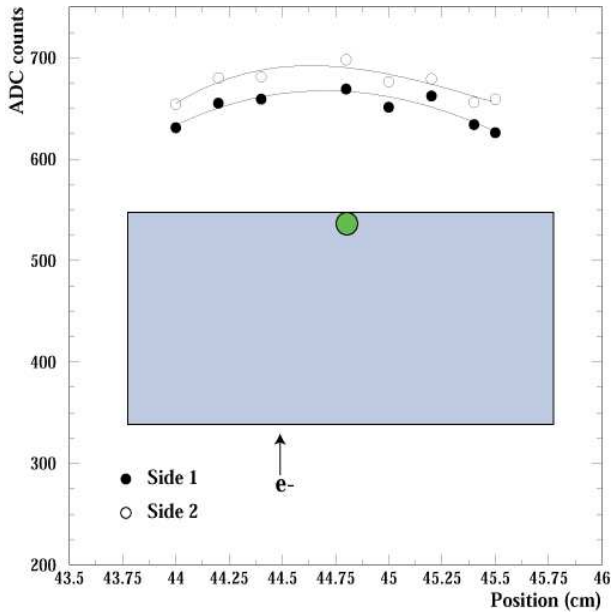

Figure 31: Signal amplitude vs beam position along the scintillator strip for a 1 cm thick and 2 cm wide strip irradiated with the electron spectrometer.

is described by a correction factor of 1.19. The electron spectrometer is a compact object. It is already available and it can be used on a movable X-Y system located over the scintillator plane to calibrate each of the 20 strips by irradiating them in their middle over a few points along their length (figure 31).

2.7.2 Photosensors and electronics calibration

The initial calibration procedure of the M64 photomultipliers is described in detail in the photomultiplier subsection. The intermediate fiber collector shown in figure 12 will also contain an LED pulsed by the DAQ card. This will allow continuous monitoring to the single photoelectron response of the photomultiplier. A charge injection system is integrated in the DAQ card in order to monitor the gains of the preamplifier chips.

3 Expected performance of the Left-Right monitor

The Left-Right monitor is meant to measure the number of neutrinos hitting its detection volume. In order to observe a possible flux asymmetry between the left and right directions, the accuracy of the measurement should be better than a few percent. The detection of ν_μ inetractions is based on the measurement of muons produced by charged current (CC) interactions and in particular charged current quasi-elastic (CCQE) scattering.

We estimated the detector performance using Monte-Carlo (MC) simulations. The `Neut` software package is used to calculate the interaction cross-section of neutrinos with nuclei in a detector. The propagation of the interaction products through the detector is simulated with GEANT4. The geometry of the monitors in the GEANT4 simulation is shown in figure 32.

In this section, we discuss the expected neutrino flux and the estimation of the interaction rates. We also present the event selection and reconstruction procedures to confirm the Left-Right monitor detection capability. The event selection efficiencies of fully contained events and partially contained events are also discussed. In addition, the expected background rates and sensitivity to the neutrino asymmetry including systematic uncertainties in the measurement are discussed as well as the possibility of detecting short proton tracks in CCQE events using the first five scintillator planes.

3.1 Beam profile

Figure 33 shows the expected flux of neutrinos hitting the Left and Right monitors. We used the latest J-PARC neutrino flux 07a[1], where the incident energy of protons was set to 30 GeV. Using `Neut` to calculate the interaction cross-section, the event rate of all muon neutrino interactions is expected to be 3.2×10^5 events/ton/year, while that of CC interactions is 2.3×10^5 events/ton/year.

As mentioned in section 2, the structure of the experimental hall restricts the possible detector positions. The Left monitor will be located 3.52 m upstream of the Right monitor along the beam direction (see figure 6). Accordingly, the height of the monitor stands are adjusted 20 cm (right) and 8 cm (left) lower than the center of the ND280 detector in order to be 2.5 degrees off-axis beam. The different distance from the beam production point produces a difference in the neutrino fluxes at both places. Figure 34 shows the neutrino flux ratio of the Right to the Left monitor. We assume that the neutrino beam is completely symmetric. The total interaction rate at the Right monitor is expected to be 3 % lower than that at the Left monitor. Since the ratio of the fluxes is relatively flat, we can correct the difference just by the relative distance. At the end we will be able to observe the effect of a few percent beam asymmetry.

The neutrino beam profile at the surface of both monitors is shown in figure 35. The profile is projected onto the vertical and horizontal axes of the surfaces perpendicular to the beam direction. The origin of the coordinate system is set to the center of each monitor. In the left figure, the on-axis line is located at -3.2 m and $+3.2$ m on the Left and the Right monitor coordinates, respectively. Since the neutrino flux depends on the detector location, a precise geometrical survey before the installation is essential. The total error due to the survey must be less than 1 cm. We calculated the variation of the flux caused by the detector location uncertainty. The flux uncertainty at ± 5 cm in the vertical direction is less than 0.5 %. Therefore, we can keep the systematic errors caused by the detector location uncertainty sufficiently small.

3.2 Event reconstruction

The determination of the muon's momentum implies the measurement of the muon range in the detector. We reconstruct the muon track by using the hit pattern of the scintillator strips. An example of a simulated CCQE interaction event is shown in figure 36. Since the scintillator strips are alternately arranged in the horizontal and vertical directions. The top and side views of the hit pattern correspond to the horizontal and vertical projections of the muon track, respectively.

A muon hit in each strip is defined by the observed energy deposition. The mean deposited energy for muons is about 2 MeV when passing through a scintillator strip. Previous studies for the muon range detector of the T2K 2KM detector show the photo electron yield of the scintillator strips to be about

[1] http://jnusrv01.kek.jp/internal/t2k/nubeam/flux/index.html

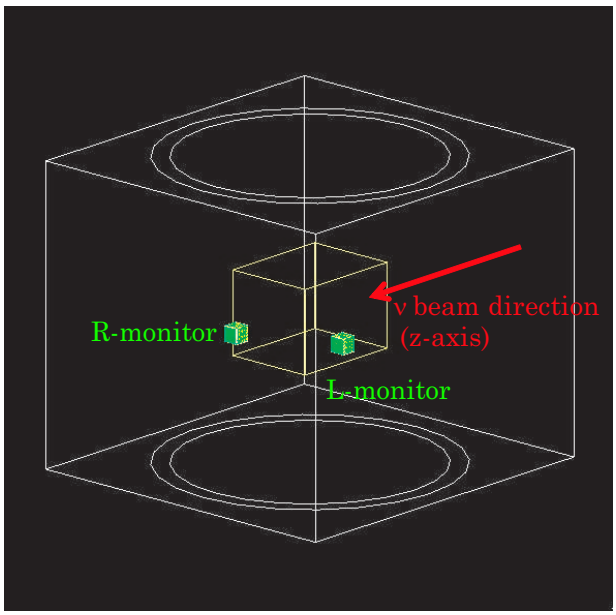

Figure 32: Geometrical location of the Left and Right monitors in the 280m detector hall in a GEANT4 event display. Both monitors are shown in green, while the magnet and the concrete walls are shown in yellow and white, respectively.

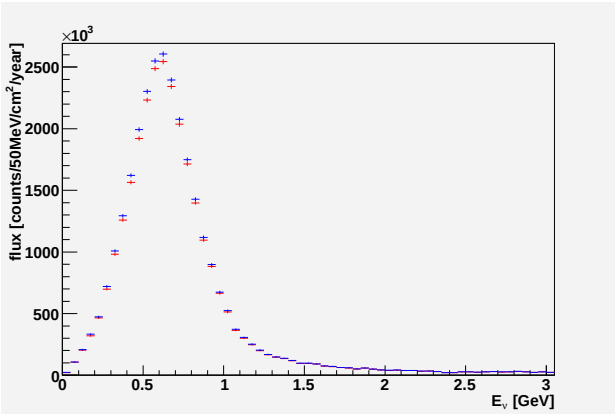

Figure 33: The expected flux of neutrinos at the location of the left (blue) and right monitor (red).

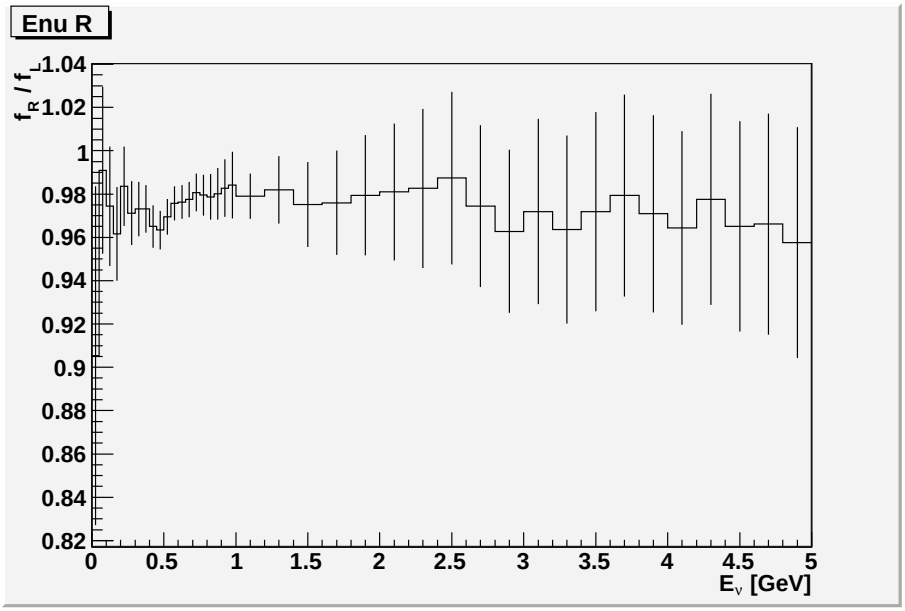

Figure 34: The asymmetry of the neutrino flux at the Right monitor to the Left monitor as a function of the neutrino energy. The large error bars in the high energy region (> 1 GeV) are due to small statistics of the flux 07a.

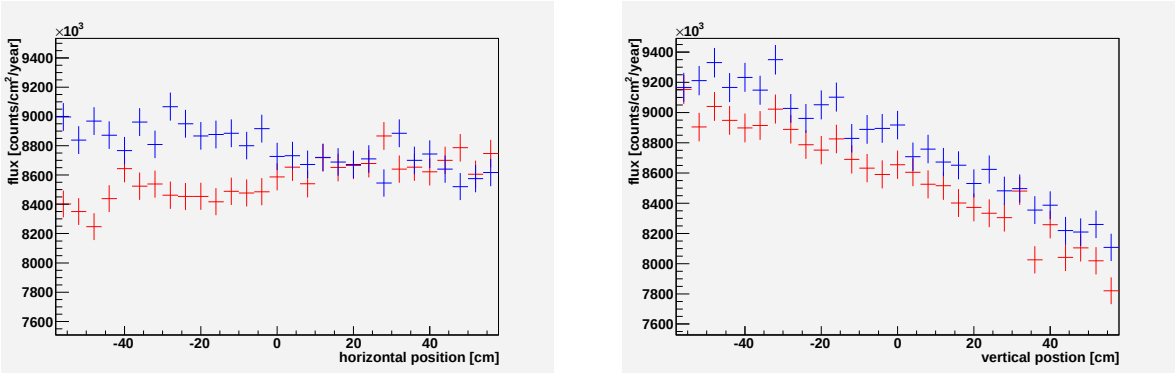

Figure 35: Neutrino beam profiles at the location of the Left monitor (blue) and the Right monitor (red). For the left picture, the on-axis line is located at -3.2 m and $+3.2$ m in the Left and the Right monitor coordinates, respectively.

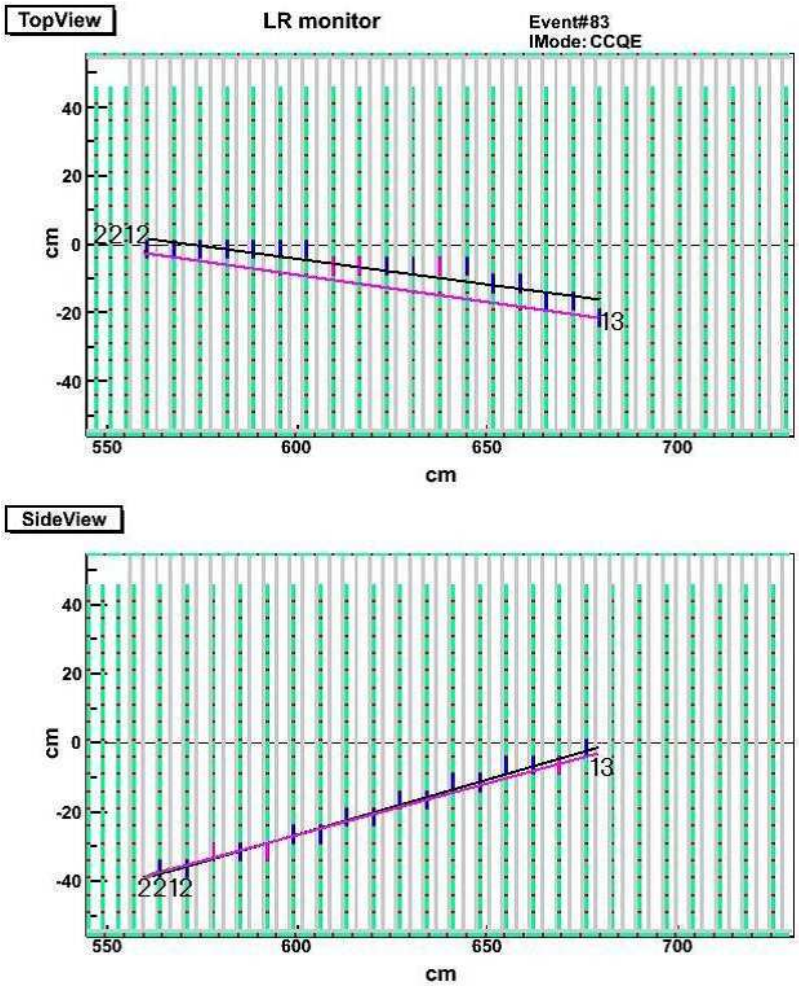

Figure 36: Event display of a typical CCQE event. Both projections are shown. The neutrino beam comes from the left-hand side. The numbers 13, 2212 and 2112 indicate the muon, the proton and the neutron, respectively. The scintillator bars with less (more) than 10 p.e. are shown in pink (blue). The reconstructed muon track is shown as a black line. The pink line is drawn from the muon interaction point to the stopping position from the "true" MC information.

6 p.e./MeV. The threshold of each strip is set to 1.5 p.e. in the simulation, where the numbers of photo electrons is smeared by the detector resolution as described in Section 2.3.

The muon range is determined by counting both the number of consecutively hit layers and by measuring the direction of the muon track. The fitted direction is shown as a black line in figure 36. The θ_x and θ_y angles with respect to the beam direction are used to calculate the angle between the track and the beam.

$$\tan^2\theta_\mu = \tan^2\theta_x + \tan^2\theta_y. \tag{1}$$

The muon range is then proportional to $N_{\mathrm{HitLayer}}/\cos\theta_\mu$, where N_{HitLayer} is the number of hit scintillator layers. At least four hit layers are required to determine the muon range. The reconstructed track is also used for the selection of partially contained events (see Section 3.5).

Comparing with the true muon momentum, we obtained the calibration function.

$$P_\mu^{\mathrm{rec}} = 15.3 \times \frac{N_{\mathrm{HitLayer}}}{\cos\theta_\mu} + 87.2\ [\mathrm{MeV}], \tag{2}$$

where the coefficient corresponds to the energy loss in each layer (1 cm of iron and a 1 cm of scintillator). Figure 37 shows the relation between the reconstructed and true muon momentum (left) and the scattering angle of the reconstructed and true muons (right) for CCQE events. The selection of fully contained and fiducial volume events is applied in this case and is further discussed in the next section.

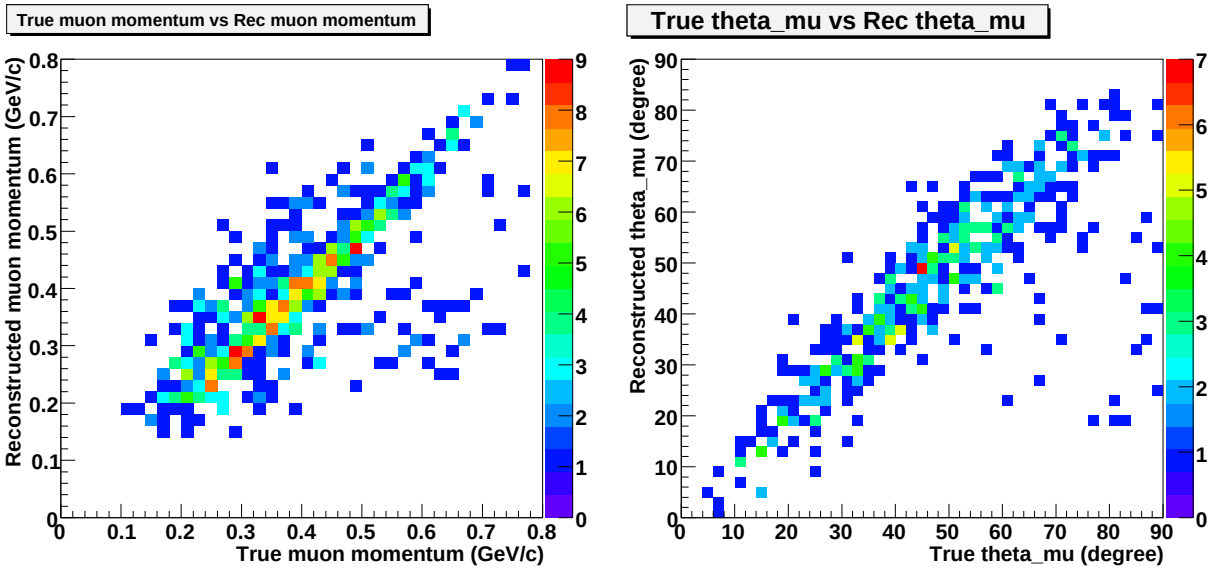

Figure 37: Relation between the reconstructed and true muon momentum (left) and the reconstructed and true angle (right). Only CCQE events are shown.

3.3 Event selection for fully contained events

In order to select events where the neutrino interacted inside the module we apply the following cuts:

- no hits in any veto scintillators (Veto cut);
- at least four consecutive hits on scintillator layers (NHitLayer) including both horizontal and vertical planes.

Figure 38 shows the number of hit counter layers after the above selection is applied. We find that the efficiency is reasonably high for CC interactions. On the other hand, most of the NC background events are rejected by the NHitLayer cut. We believe that the low NC contamination could be experimentally proven once neutrino interactions are precisely measured by the ND280 detector.

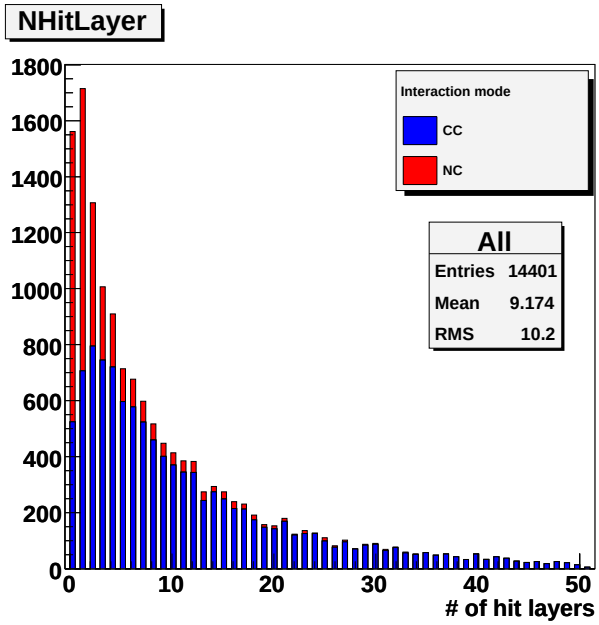

Figure 38: The number of hit counter layers for both CC (blue) and NC interactions (red).

In addition, we can apply a fiducial volume cut to reduce background induced by neutrons generated outside the detector. Muons, neutrons or gamma rays are expected to sneak into the Left-Right modules. Based on a detailed study of the background we define two different fiducial volumes depending on the number of hit layers and summarize them for three event categories in table 6:

Event category	1	2	3
NHitLayer	4-6	7-9	$\geq$10
fiducial volume (size)	FV 2 (80×80×144.5 cm^3)	FV 2 (80×80×144.5 cm^3)	FV 1 (90×90×151.5 cm^3)

Table 6: Summary table for the fiducial volume cut. Event category 1 requires that the mean number of p.e.>30 if 70<the maximum number of p.e.<160 or the mean number of p.e.>25 if the maximum number of p.e.<70. The maximum p.e. cut (<160) is applied to remove neutron background. Event category 2 requires that the total number of p.e.>120. The p.e. cut (>120) is applied to reduce the γ ray background from outside interactions.

FV 1 and 2 are the fiducial volume shown in the red region in figure 39. In FV 1(2), the events in 12(14) upstream scintillator layers along the z-axis and 1(2) scintillator bar(s) at both ends of each horizontal and vertical layers on the x and y-axes are rejected. Events falling in one of three categories above are selected as fully contained events.

Figure 40 shows the true neutrino energy spectrum with and without the selection for all neutrino interactions (left) and only CC interactions (right). Neutrinos in the high energy tail above 1 GeV are rejected by the veto. However, most of the ν_μs have a momentum lower than 1 GeV. In addition, since the energy range relevant to oscillations is the one below 1 GeV, the Left-Right detector is expected to cover this energy region.

The muon momentum distribution of CC interaction is shown in figure 41. In the right figure, CC events are separated into CCQE, CC1π and other CC interactions. Compared with the CCQE events, muons from other CC events have relatively low momentum. This is due to the energy carried away by other particles produced in the interaction.

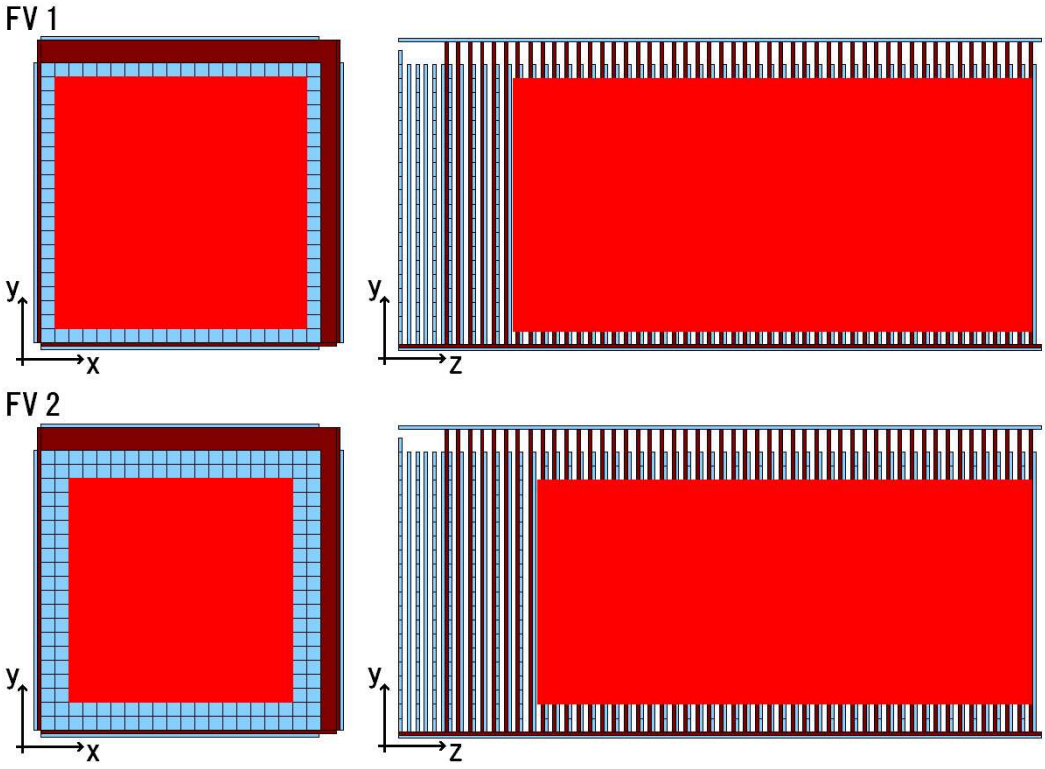

Figure 39: The fiducial volumes in Event category 1 (top), and Event categories 2 and 3 (bottom) are shown in red for the detector front (left) and side view (right).

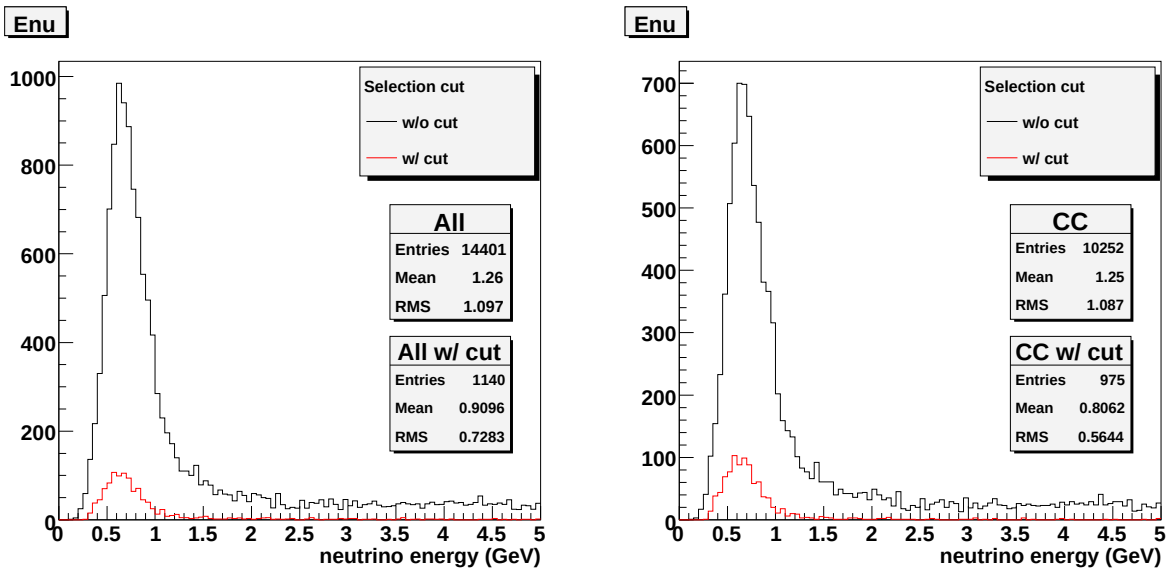

Figure 40: True neutrino energy spectrum for all (left) and CC (right) events at the Left-Right monitor position in the 280m detector hall. The black histogram shows events without any cuts, while the red histogram shows events passing the selection criteria discussed in the text.

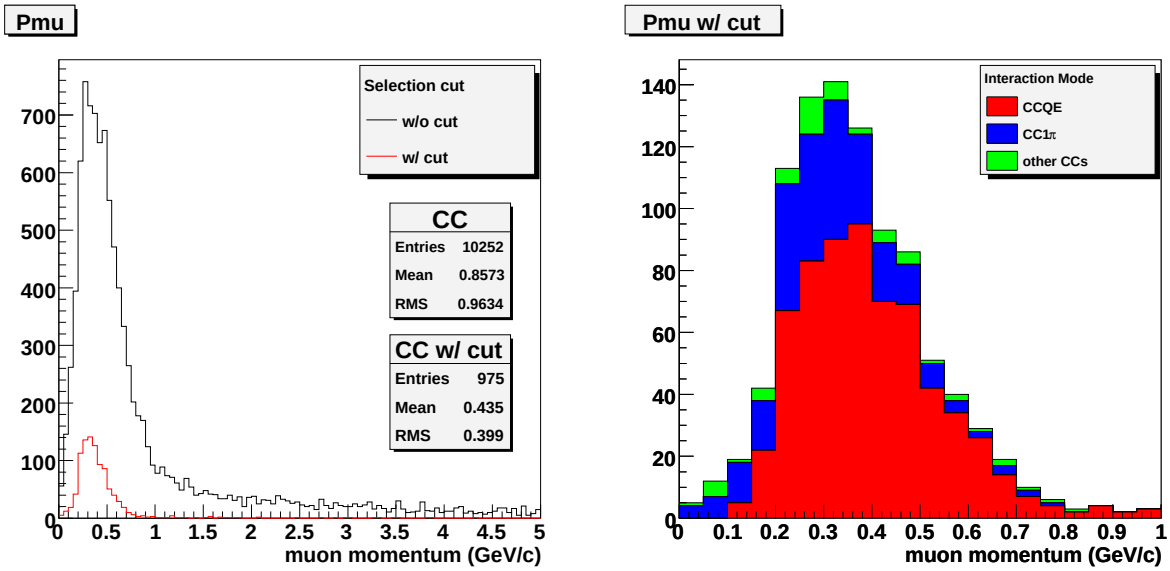

Figure 41: Left: true muon momentum distribution without any selection cut (black) and with all the cuts applied. Right: the distribution for each interaction mode (CCQE, CC with single π, others) is shown as a function of the muon momentum after the selection cuts.

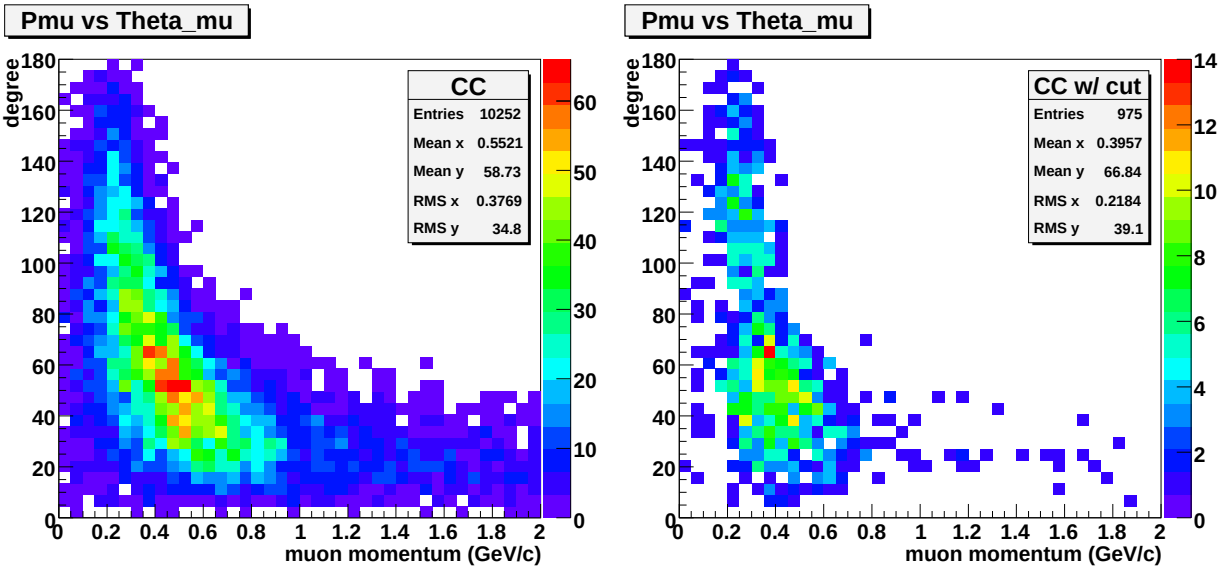

Figure 42: The muon scattering angle as a function of momentum with no selection cuts applied (left) and with all the cuts (right). A large fraction of the higher muon momentum events ($>$ 800 MeV) are rejected by the cuts. These muons have a rather small scattering angle but are rejected because by the veto cut.

Figure 42 shows the muon scattering angle as a function of the muon momentum with no cuts (left) and with all the selection cuts applied (right). Lower momentum muons (< 500 MeV) tend to be scattered at a large angles (20 to 140 degrees), and they are often rejected by the veto cut. Events with a higher muon momentum(> 800 MeV) are also largely rejected. These muons have a relatively low scattering angle, but don't stop inside the module due to the small detector size. Therefore, muons can go through and hit the veto counters at the downstream side of the module. The remaining events in the high momentum region have muons that can either escape veto tagging or go through gaps between consecutive scintillator bars.

We summarize the event selection efficiency in table 7. Due to the detector's limited size, events near the walls don't remain in the active volume and therefore the detection efficiency after the veto cut is reduced by 70 %. We want to stress that the data from the other ND280 detectors will be very important to confirm our estimates of the Left-Right monitor efficiency as a function of the muon momentum and the scattering angle.

Table 7: Number of events in one module with all FC cuts applied. One year of running (120 days) is assumed.

	All : 986674 events				CCQE : 366184 events			
NHitLayer	4-6	7-9	$\geq$10	Total	4-6	7-9	$\geq$10	Total
interaction	153266	110651	335035	598952 (100 %)	69622	52702	140094	262418 (100 %)
veto	56045	35079	71803	162927 (27.2 %)	22075	15162	38389	75626 (28.8 %)
FV cut	16101	17403	44603	78107 (13.0 %)	6974	7702	24926	39602 (15.1 %)
efficiency	10.5 %	15.7 %	13.3 %	13.0 %	10.0 %	14.6 %	17.8 %	15.1 %

3.4 Background estimation

Since the Left-Right monitor is planned to be installed in the most downstream part of the ND280 area, neutrino interactions in the upstream components can induce a large number of background events. Daughter particles from these events can contaminate the fully contained events, producing some uncertainty in the ν flux measurement. Hits in the veto planes may cause dead time in the Left-Right monitor.

The backgrounds mentioned above depends on the actual location of the Left and Right modules. Therefore, we must understand and evaluate them for each module, separately. For this purpose we generated neutrino interactions inside the magnet and the concrete wall.

The following two event samples are prepared using the simulated events in order to evaluate the effect of background;

- fully contained (FC) event selection as described in the previous subsection
- $N_{\mathrm{veto}} > 0$

where N_{veto} indicates the number of hits in the veto scintillators. The first sample is to estimate the contamination rate of the background events, and the second sample is to estimate the inefficiency due to hit rate on the veto scintillators.

Figure 43 shows the vertex distribution after the standard FC selection. Background events originating in the magnet mostly affect the Right monitor, while events in the concrete contribute to the Left monitor backgrounds. The number of remaining background events after the selection cuts are summarized in table 8. The background contamination is expected to be 1.5 % for the Right-monitor and 2.0 % for the Left-monitor. The main message is that background events are effectively suppressed by our fully contained event selection.

In order to evaluate the uncertainty on this background estimation, we produced a control sample whose background rate is larger than that of the standard FC selection. The normalization and its uncertainty is determined by comparing the numbers of selected events from the standard FC with the control data sets. To avoid systematic biases, the control sample is defined as the events that survive almost the same selection criteria as for the standard FC selection. The only difference is the fiducial cut: events whose muon candidate track starts between the 7th and 12th layers are selected to belong to the control sample. The numbers of the control sample events are also summarized in table 8.

The relation between the number of selected events (standard cuts) and the control sample events is described by the following equations:

$$\begin{aligned} \mathbf{N}_{\mathrm{regular}} &= N^{sig}_{regular} \cdot x + N^{BG}_{regular} \cdot y \\ \mathbf{N}_{\mathrm{control}} &= N^{sig}_{control} \cdot x + N^{BG}_{control} \cdot y \end{aligned} \tag{3}$$

where x and y are normalization factors for signal and background simulated events, $N^{sig}_{regular}$, $N^{sig}_{control}$, $N^{BG}_{regular}$ and $N^{BG}_{control}$ indicate the numbers of signal and background events after applying the standard and control sample selections (we use the values in table 8). $\mathbf{N}_{\mathrm{regular}}$ and $\mathbf{N}_{\mathrm{control}}$ denote the number of events after applying each selection. The uncertainty on the background MC normalization, $\Delta y/y$, is determined from the statistical uncertainty of $\mathbf{N}_{\mathrm{regular}}$ and $\mathbf{N}_{\mathrm{control}}$. The resulting uncertainties on the estimated number of background events are 9.1 % and 4.0 % for Right-monitor and Left-monitor, respectively, for one year of running.

We must also consider the rate of multi-interaction events, since it causes inefficiency in the signal selection. We reject fully contained events if the external particles hit the veto counter at the same time. This effect is also studied by applying the second selection criterion, $N_{\mathrm{veto}} > 0$. We then estimate 0.053 and 0.029 veto hit events per spill for the Right-monitor and the Left-monitor, respectively. Since a spill from the T2K beam consists of 8 bunches, each $\sim$ 50 ns long and $\sim$ 500 ns apart, we can only veto one bunch whose timing corresponds to the timing of a veto hit in a spill. Therefore, the dead time becomes 0.7 % for the Right-monitor and 0.4 % for the Left-monitor.

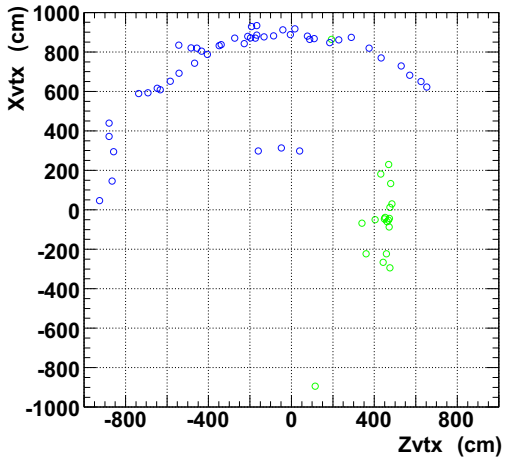

Figure 43: Vertex distribution after regular FC selection: The distributions of events selected by Right- and Left-modules are shown by green and blue open circles, respectively.

Table 8: Signal and background events (from interactions in the magnet and in the concrete wall) before and after selection criteria have been applied (see the text for explanation). We assume one year of running.

	ν interaction	no. of regular FC events	no. of control sample events
R-monitor (signal)	9.9×10^5 (event/year)	78107 (event/year)	16465 (event/year)
R-monitor (BG)	6.8×10^8 (event/year)	1177 (event/year)	1907 (event/year)
BG/signal ratio	692	0.015	0.116
L-monitor (signal)	9.9×10^5 (event/year)	78107 (event/year)	17471 (event/year)
L-monitor (BG)	6.8×10^8 (event/year)	1584 (event/year)	4482 (event/year)
BG/signal ratio	692	0.020	0.257

3.5 Partially contained events

The selection criteria described in Section 3.3 eliminates a large fraction of CC events. As shown in figure 41, the detection efficiency around 400 MeV/c is about 20 %. This is mainly due to hits in the side and back veto scintillator planes. Furthermore, almost all muons above 1 GeV are not fully contained due to the limited size of the detector. Though the significant energy region for our measurement is below 1 GeV, it is useful to measure the asymmetry in the higher energy region as well. To increase the efficiency and the statistics especially in this region, we also considered partially contained (PC) events.

PC muons may interact inside the detector and escape leaving a veto hit. We apply the following criteria for PC events:

- there is a veto hit;
- NHitLayer ≥ 4;
- Fiducial volume cuts described in Section 3.3.

Figure 45 shows a typical PC event from a CCQE interaction. The reconstructed track (black line in the figure) passes through one of the veto strips. To discriminate a muon veto hit from an accidental coincidence, we extrapolate the reconstructed muon track and searched for corresponding hits on the veto strip intersecting the track or in two adjacent strips.

As described in Section 3.4, neutrinos that interact outside the Left-Right monitor, in the concrete wall or in other ND280 detector components, for instance, can be a source of background. However back-scattered muons exiting a module with a veto hit show similar hit patterns. An example of a back-scattered

muon is shown in figure 45. The timing resolution of the readout system is not enough to distinguish whether the muon comes from inside or outside. In order to not misidentify back-scattered muon as background, the veto hit position is compared with the counter layer hit positions. If the veto hit is upstream of the counter layer hit, i.e., the veto hit is closer to the beam source, the event is rejected. This is necessary because most background muons first hit the veto counter and then leave tracks in the counter layers. As shown in figure 42 (right), most of back scattered muons (angle between scattered muon and incident neutrino $\geq$ 90 degree) have small momentum. Therefore, only a small fraction of the back scattered muons hit the veto planes.

Neutrinos above 1 GeV can be considered as a control sample to estimate the difference between the NC background rates in the Super-K and in the 2KM water Cherenkov detectors. In order to select only high energy PC events, we define the following selection criteria:

- the muon scattering angle must be smaller than 70 degrees (see figure 42). This rejects most back-scattered muons;
- NHitLayer is larger than 30, as required to select high momentum muons.

These cuts can eliminate low energy PC events, while retaining neutrinos above 500 MeV.

We summarize the efficiency for fully contained (FC), PC and high energy PC events in table 9. The detection efficiency decreases by about 1 % after discarding back-scattered events. The statistics including PC events become about three times larger than that of only FC events. Figure 44 shows the neutrino energy spectrum and muon momentum for FC, PC and high energy PC events.

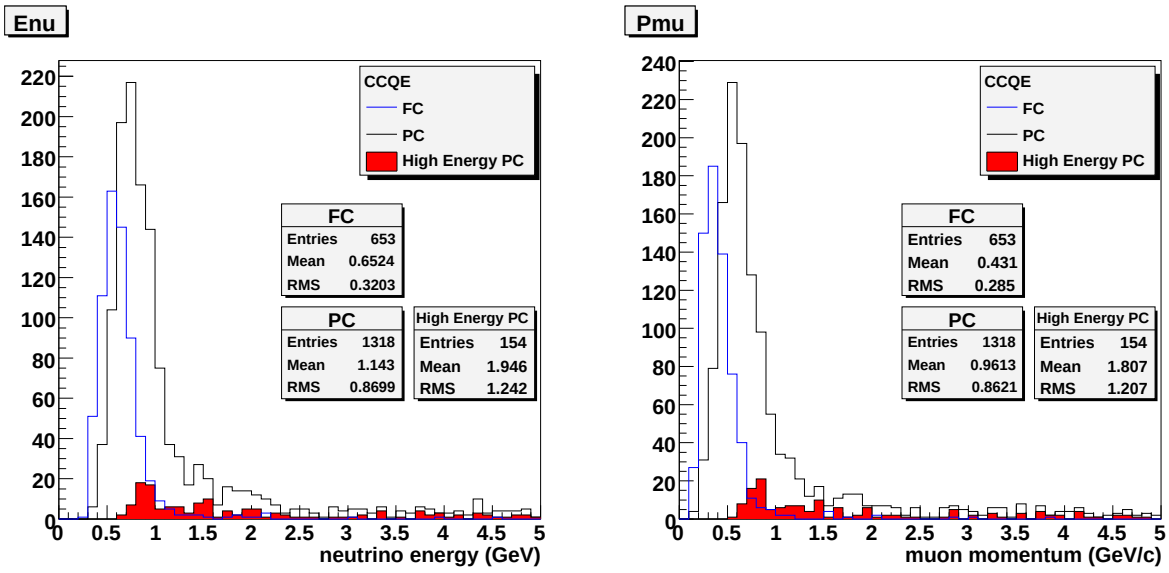

Figure 44: The neutrino energy and muon momentum spectrum for FC, PC and high energy muon PC events.

Table 9: The number of events and detection efficiency for FC and PC events. 1 year running time is assumed.

Event	CCQE	Efficiency
FC	39602	15.1 %
PC	79932	30.5 %
high energy PC	9340	3.6 %
FC + PC	119534	45.6 %

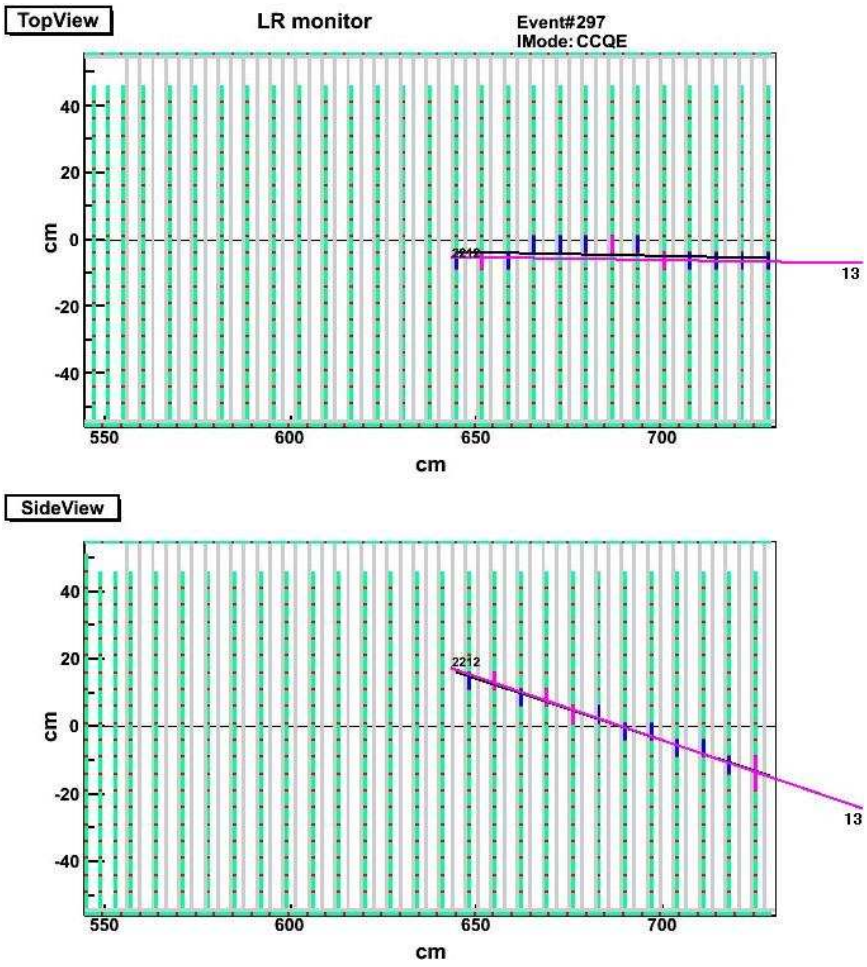

Figure 45: Display of a typical CCQE PC event. The pink and black lines show the true and reconstructed muon tracks, respectively.

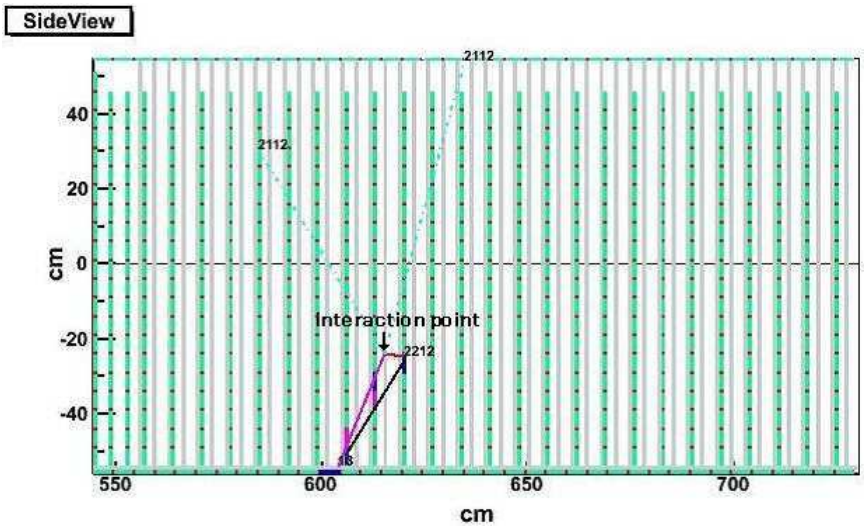

Figure 46: Display of a typical back-scattered muon event. The scattered muon (with a relatively large angle) and hits a veto counter.

3.6 Upstream events

The Left-Right monitor modules have 5 layers of scintillator planes without any passive material (iron plates) in their upstream part. All the deposited energy can then be measured in these detection volumes. However it is basically impossible to observe short range particles (such as a recoiling proton or nucleus) in the volume with just the iron plates. For example, most of the protons produced in CC interactions in an iron plate can not reach a scintillator strip delivering a detectable signal. The upstream active volume can be used to study the propagation of short range particles. In particular, the measurement of a proton accompanied by a muon allows us to distinguish CCQE events from NC and other types of CC events. For CCQE events, the momentum and the scattering angle of protons are determined by the reconstructed muon kinematics. This analysis is useful to reduce the systematic uncertainty on the contamination of non-CCQE events in the fiducial volume that would otherwise strongly depend on simulations.

Figure 47 shows a CCQE event in the upstream volume. Both the muon and proton tracks are clearly visible and separated from each other. The momentum of the proton can then be estimated from the deposited energy in the scintillator planes and from the range of the track.

We set the following selection criteria in order to measure the energy and the direction:

- tracks are fully contained in the detector;
- the angle between the muon and the proton track is between 50° and 140° (Angle cut);
- NHitLayer for the proton is larger than 4.

The distribution of the angle between the muon and the proton tracks as a function of the number of hit scintillator layers for the proton is shown in figure 48. The mean value of the angle is about 100°, which is sufficiently large for clear separation of the tracks. As shown in the figure, most of the events have less than four hits, thereby preventing the proton track from being clearly identified over background. However in order to hit four layers, the momentum must be higher than 350 MeV/c (corresponding to a kinetic energy of 60 MeV).

We can summarize the expected statistics in table 10. About 200 events per year can be collected, almost all of them CCQE events.

Table 10: The number of events occurring in the upstream volume of the modules after the selection criteria. One year running time is assumed.

CCQE	number of events
interaction	4394
+ FC	775
+ Angle cut	678
+ NHitLayers	204

3.7 Sensitivity to the beam asymmetry

We evaluated the sensitivity to the left-right symmetry by comparing the measured ν_μ beam flux between the Left- and the Right-module in two ways; the total number of events in a module and events as a function of neutrino energy.

The simple way to estimate the left-right symmetry is to compare the number of selected events in each module. The sensitivity, $\Delta r/r$, is shown as a function of the running days in figure 49, where r is the measured asymmetry derived by the ratio of the response of the Left- to the one of the Right-monitor. For FC, high energy PC, and FC+PC events these are estimated by their selection efficiencies. The systematic uncertainty as well as the statistical uncertainty are considered for these results. Most of the systematic uncertainties in the flux measurement cancel since the Left- and Right-modules have an identical structure and we apply the same kinematic reconstruction and event selection on them. Only uncertainties in the background estimation and the accuracy in the measurement of the detector positions

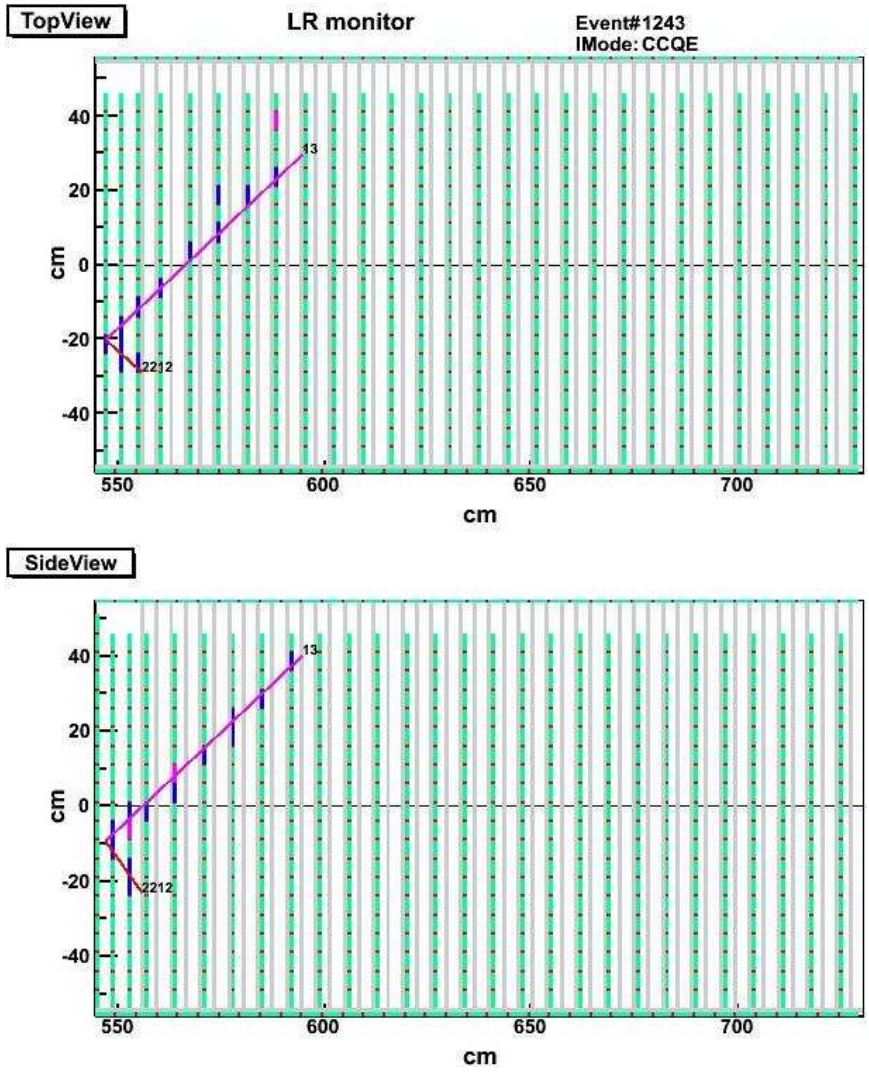

Figure 47: Display of a typical CCQE event with a visible proton track in the upstream volume of the module. Fully contained tracks of the muon and the proton can be clearly identified.

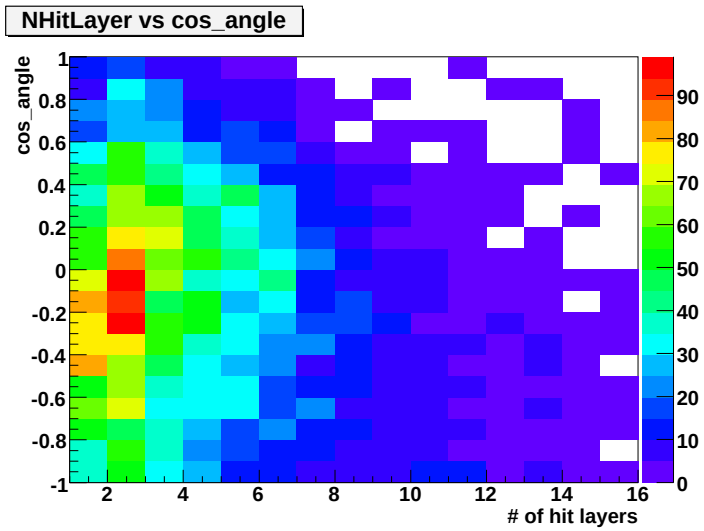

Figure 48: The distribution of the angle between the muon and the proton tracks for CCQE events with a visible proton track.

contribute to the systematic uncertainty in the flux ratio. As described in Section 3.4, the uncertainty in the background estimation is smaller than 10 % and the background contamination for each signal sample is small. Therefore, the systematic uncertainty in the background estimation is negligible. The difference in efficiency caused by varying the expected flux when we move the module ± 5 cm in x, y, and z directions, is estimated to be at most 0.5 %. We assumed the latter as the detector position systematic uncertainty. The sensitivity of the ratio for FC+PC events could reach 2 % in only 3 days of operation. The symmetries of both low energy and high energy parts of the ν_μ flux can be studied with FC and high energy PC events. The sensitivity to FC events could be less than 2 % and for high energy PC events less than 5 % in only 10 days of operation.

The left-right symmetry dependence on the neutrino energy is important information for the oscillation analysis of the T2K experiment. By using the Left-Right monitor we can measure it with a sensitivity better than the sensitivity on the flux measurement performed by the 2KM detector. The energy of the incoming neutrino can be reconstructed for CCQE events by:

$$E_\nu = \frac{1}{2} \cdot \frac{2M_p E_\mu - M_\mu^2}{M_p - E_\mu + \sqrt{E_\mu^2 - M_\mu^2} \cdot \cos\theta_\mu}, \tag{4}$$

where M_p and M_μ are the masses of proton and muon, respectively. E_μ and θ_μ are the energy and the scattering angle of the final state muon.

The E_ν distribution and efficiency curve for CCQE events after one year of running are shown in figure 50. The systematic uncertainty and the total uncertainty assuming 30 days and one year of running are shown as a function of E_ν in figure 51. The systematic uncertainties in the background estimation and in the detector position are taken into account for this study. The systematic error in the estimation of background events becomes ~ 5 % for the low energy region, since most of the background events populate this energy region. The total uncertainty becomes 5 % between 300 and 800 MeV with 30 days of running and becomes smaller than 5 % with one year of running. This performance is better than the one we expect from the 2KM detector complex.

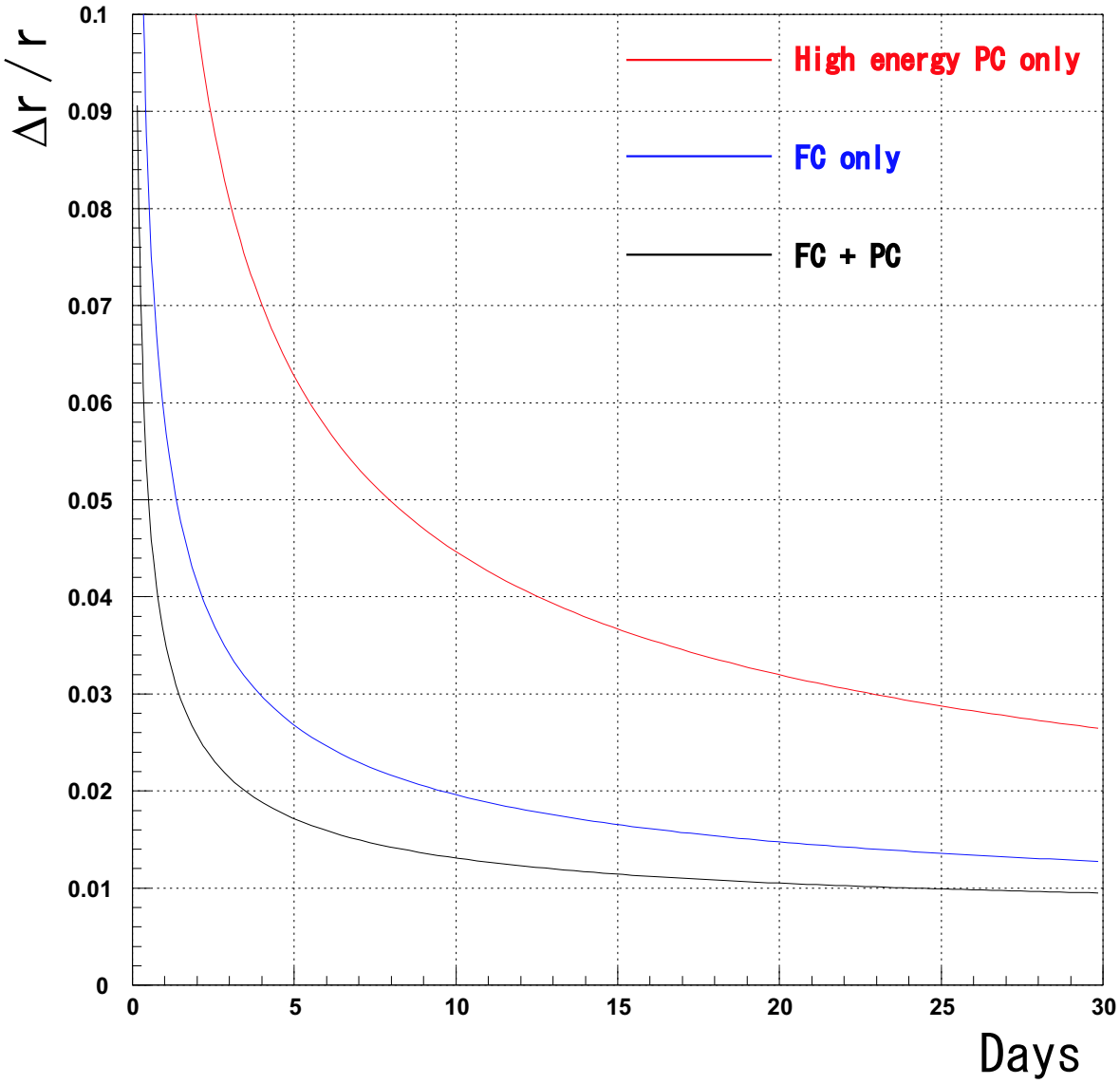

Figure 49: Sensitivity in the asymmetry measurement $\Delta r/r$ as a function of the days running. The sensitivity is shown for FC+PC (black), high energy PC only (red) and FC only (blue) events.

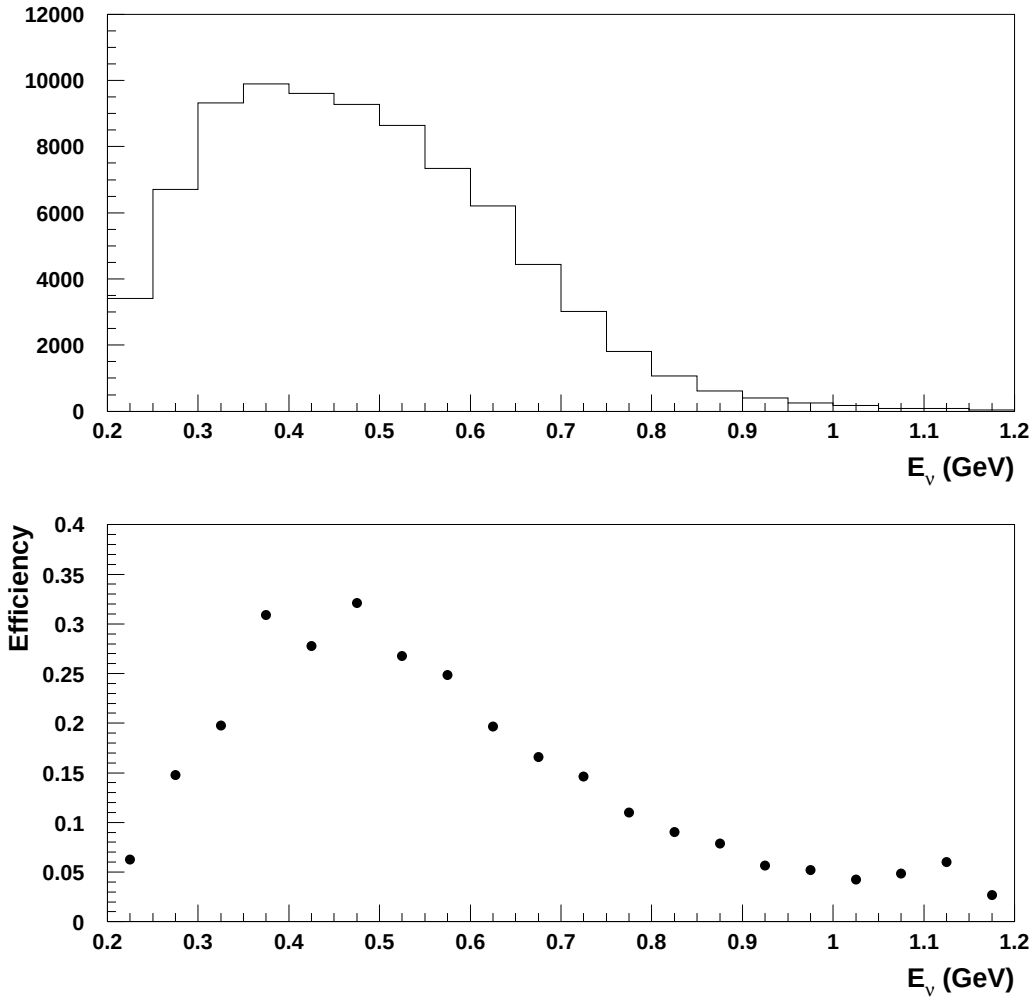

Figure 50: The reconstructed E_ν distribution for CCQE events assuming one year of running (top) and the corresponding efficiency curve (bottom).

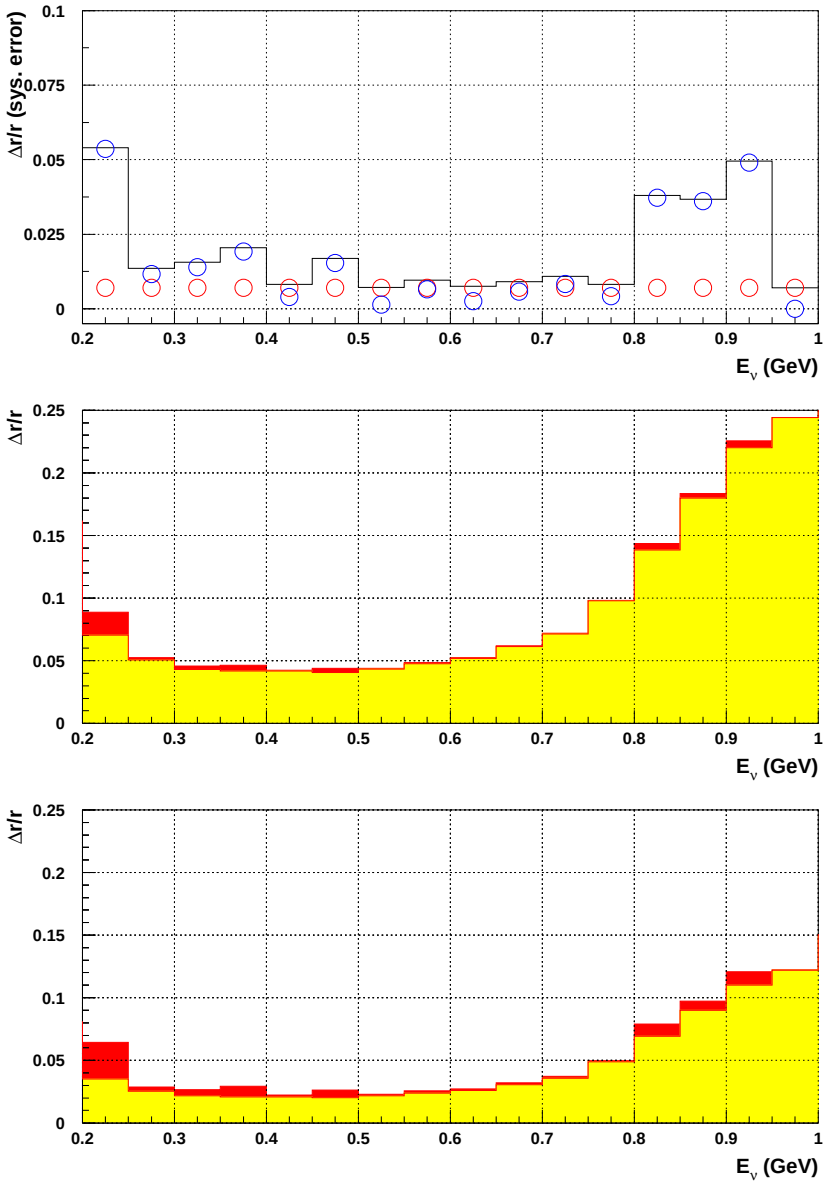

Figure 51: The relative systematic uncertainties in the Right- to Left-monitor flux ratio (top): uncertainties in the background estimation and in the detector position are shown by blue and red circles, respectively. The total systematic uncertainty is shown by the histogram, the relative uncertainty in the determination of the flux rate is shown in the middle (bottom) plot for a running period of 30 days (one year). The yellow histogramm indicates the statistical error while the red one shows the total uncertainty.

4 Construction and installation schedule

The details of the Left-Right monitor design will be settled soon. We plan to build a counter plane made of 20 scintillator bars in order to confirm the assembly procedure, confirm the design features, take cosmic-ray data with a multianode PMT readout chain including the software to control the DAQ system, check light tightness and cross talk and test the calibration system with a ^{90}Sr source. This test is scheduled for 2-3 weeks in late October 2008.

In parallel, seismic hazard simulations for the detector will be performed. The design of the detector stands and the mechanical structure will be finalized after these simulations. This will be done at ICRR in late 2008.

The electronics boxes will be designed and built in Lyon by the end of 2008.

We will start mass production of the counter planes in Bern early 2009. The planes will then be shipped to ICRR in August 2009.

All the electronics will be prepared in Lyon by March 2009. These will be tested in April with the counter planes in Bern. The counter planes will then be inserted in the mechanical structure, the electronics boxes will be mounted on the top of the modules and optical fibers will be routed into them at ICRR. Both Left and Right monitor will be assembled at the same time at ICRR.

We plan to install the Right monitor at the downstream magnet site if all ND280 detector components are installed and if there is no conflict with the ND280 schedule. In order to minimize the access time to the hall we will complete the detector assembly at ICRR and ship the modules to J-PARC just before installation. The Left monitor will be installed if the ND280 magnet is not expected to be opened frequently.

The schedule for assembling, testing and installing the Left-Right monitor is summarized below.

FY 2008

- Finalize the detector design.
- Most of the detector elements will be purchased this year and shipped to Bern.
- Make a prototype of a counter plane. Verify the mass production procedure.
- Test the counter plane with cosmic-rays using the final electronics and DAQ systems.
- Start building the detector stands and the mechanical structure at ICRR as well as the electronics boxes in Lyon.

FY 2009

- Start mass production, testing and calibration of the tracking planes in Bern.
- Ship the tracking planes and the readout systems to ICRR.
- Assemble the module with the mechanical structure and the full readout systems at ICRR.
- Install the Right module in the ND280m hall if there is no conflict with the other detectors' installation schedule.

FY 2010

- Install the Left monitor if the ND280 magnet is not expected to be opened frequently.

A last word about the funding of the detector. All detector components, manpower and related equipment are fully funded. The required resources for the detector installation and operation are also funded.

References

[1] T2K collaboration, "A letter of intent to extend T2K with a detector 2 km away from the J-PARC neutrino source", http://neutrino.cgi.phy.duke.edu/2km/wiki/.

[2] Alan Grant, "Preparation for Installation", T2K collaboration meeting, Jan. 12, 2008.

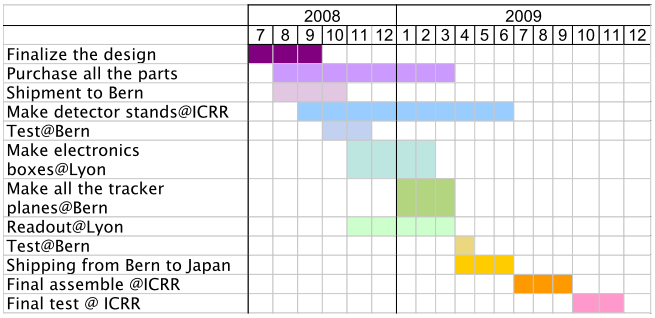

Figure 52: The construction schedule of the Left-Right monitor detector.

[3] "Document for 280m review", http://www.nd280m.org/info.

[4] "Performance of a FE electronics ASIC for the OPERA Target Tracker: Version-1", Opera Internal note #34

[5] "Performance and Design of a Front End electronic ASIC for the OPERA Target Tracker: Version-2", Opera Internal note #40

[6] "The OPERA ROC: a Read Out Chip for the OPERA Target Tracker", Opera Internal note #41.

[7] "The scintillator option for the OPERA target tracker: results on the readout", L.Chaussard et al, OPERA internal note, July 06, 2001.